Corresponding Author: Dr. John Thomas Caulfield, PhD

Corresponding Author's Institution: Queensland University of Technology

First Author: John Thomas Caulfield, PhD

Order of Authors: John Thomas Caulfield, PhD; Emma L Tomlinson; David M Chew; Michael A Marks; Cora A McKenna; Teresa Ubide; Victoria C Smith

Abstract: Constraining the abundance and distribution of halogens in geological materials has the potential to provide novel insights into a broad range of earth system processes (e.g. metasomatism, melting, volatile cycling and ore formation). In this contribution we develop analytical protocols for the in situ measurement of Cl, Br and I in widely distributed standard reference materials (apatite, scapolite, silicate glass) using readily available laser ablation ICP-MS instrumentation. Ablations were performed at a range of square spot sizes (30 - 80 µm) using a high repetition rate (25 Hz) and extended analyte dwell times (up to 250 ms) to improve sensitivity and signal stability. A comparison of LA-ICP-MS results with published halogen data was used to calculate the following theoretical limits of quantification; Cl = 360 µg/g, Br = 8 µg/g, I = 0.75 µg/g. A detailed assessment of raw signal intensities for different matrices with known halogen contents, combined with high resolution mass scans, provides new constraints on the origin of apparent halogen signals: on mass ^{35}Cl signal excesses are likely $^{16}O^{18}OH$ and/or $^{17}O^{18}O$; ^{79}Br is influenced by peak shoulder overlap from $^{40}Ar^{40}Ar$ (a diargon cation, Ar_2^{+2}) and a matrix-based interference ($^{159}Tb^{2+}$) for samples with Br/Tb <0.6; ^{127}I signals are similar for all but the highest I materials analysed here, suggesting the presence of ubiquitous gas-based interferences. The observation that false positive halogen signals only occur during sample ablation suggests that they are either matrix derived or related to the process of sample introduction. During ablation, matrix loading may reduce plasma energy, resulting in a greater proportion of polyatomic interferences in the system. For Cl, we provide a new time dependent excess apparent Cl spline correction defined by analysis of halogen-free olivine via a modified version of the Iolite Data Reduction Scheme 'X_Trace_Elements_IS'. The correction improves the limit of linearity to ~100 µg/g for Cl in glasses down to a 38 µm spot size. We test our methodology on apatite from Permian alkaline lamprophyres in the Pyrenees (Spain) and quartz-hosted melt inclusions from rhyolitic deposits at the Taupo volcanic zone (New Zealand), obtaining results comparable to electron microprobe and SIMS data. We provide recommendations for analytical best practice and highlight the

need for well characterised matrix matched SRMs spanning a broad range of concentrations to allow for the identification and removal of non-analyte related contributions to measured signals.

Research Data Related to this Submission

Title: Data for: Microanalysis of Cl, Br and I in apatite, scapolite and silicate glass by LA-ICP-MS
Repository: Mendeley Data
https://data.mendeley.com/datasets/7svt3gc53g/draft?a=a5aa46c0-7425-4b39-ad34-e3738781d59b

Microanalysis of Cl, Br and I in apatite, scapolite and silicate glass by LA-ICP-MS

John T. Caulfield[ab]*, Emma L. Tomlinson[a], David M. Chew[a], Michael A.W. Marks[c], Cora A. McKenna[a], Teresa Ubide[d], Victoria C. Smith[e]

[a]Department of Geology, School of Natural Sciences, Trinity College Dublin, Dublin 2, Ireland
tomlinse@tcd.ie
chewd@tcd.ie
mckennc6@tcd.ie
[b]Central Analytical Research Facility, Institute for Future Environments, Queensland University of Technology, 2 George St, Brisbane 4000, Queensland, Australia
john.caulfield@qut.edu.au
[c]FB Geowissenschaften, Universität Tübingen, Wilhelmstrasse 56, D-72074 Tübingen, Germany
michael.marks@uni-tuebingen.de
[d]School of Earth and Environmental Sciences, The University of Queensland, Brisbane QLD 4072, Australia
t.ubide@uq.edu.au
[e]Research Laboratory for Archaeology and the History of Art, School of Archaeology, University of Oxford, 1 South Parks Road, Oxford, OX1 3TG, UK
victoria.smith@arch.ox.ac.uk

*Corresponding author: john.caulfield@qut.edu.au

48   **Abstract**

49   Constraining the abundance and distribution of halogens in geological materials has

50   the potential to provide novel insights into a broad range of earth system processes

51   (e.g. metasomatism, melting, volatile cycling and ore formation). In this contribution

52   we develop analytical protocols for the *in situ* measurement of Cl, Br and I in widely

53   distributed standard reference materials (apatite, scapolite, silicate glass) using readily

54   available laser ablation ICP-MS instrumentation. Ablations were performed at a range

55   of square spot sizes (30 – 80 μm) using a high repetition rate (25 Hz) and extended

56   analyte dwell times (up to 250 ms) to improve sensitivity and signal stability. A

57   comparison of LA-ICP-MS results with published halogen data was used to calculate

58   the following theoretical limits of quantification; Cl = 360 μg/g, Br = 8 μg/g, I = 0.75

59   μg/g. A detailed assessment of raw signal intensities for different matrices with

60   known halogen contents, combined with high resolution mass scans, provides new

61   constraints on the origin of apparent halogen signals: on mass ^{35}Cl signal excesses are

62   likely $^{16}O^{18}OH$ and/or $^{17}O^{18}O$; ^{79}Br is influenced by peak shoulder overlap from

63   $^{40}Ar^{40}Ar$ (a diargon cation, Ar_2^{+2}) and a matrix-based interference ($^{159}Tb^{2+}$) for

64   samples with Br/Tb <0.6; ^{127}I signals are similar for all but the highest I materials

65   analysed here, suggesting the presence of ubiquitous gas-based interferences. The

66   observation that false positive halogen signals only occur during sample ablation

67   suggests that they are either matrix derived or related to the process of sample

68   introduction. During ablation, matrix loading may reduce plasma energy, resulting in

69   a greater proportion of polyatomic interferences in the system. For Cl, we provide a

70   new time dependent excess apparent Cl spline correction defined by analysis of

71   halogen-free olivine via a modified version of the Iolite Data Reduction Scheme

72   'X_Trace_Elements_IS'. The correction improves the limit of linearity to ~100 μg/g

73 for Cl in glasses down to a 38 μm spot size. We test our methodology on apatite from

74 Permian alkaline lamprophyres in the Pyrenees (Spain) and quartz-hosted melt

75 inclusions from rhyolitic deposits at the Taupo volcanic zone (New Zealand),

76 obtaining results comparable to electron microprobe and SIMS data. We provide

77 recommendations for analytical best practice and highlight the need for well

78 characterised matrix matched SRMs spanning a broad range of concentrations to

79 allow for the identification and removal of non-analyte related contributions to

80 measured signals.

81

82 **Keywords**

83 Laser ablation ICP-MS, halogens, apatite, scapolite, silicate glass, polyatomic

84 interferences

85

86 **1. Introduction**

87 Halogens influence fundamental magma properties such as melting behaviour and

88 melt rheology, and so affect the mobility of melts (e.g. Baasner et al., 2013). Halogens

89 also affect and track the distribution of other volatile species and incompatible

90 elements amongst the Earth's geochemical reservoirs (Kendrick et al., 2014b;

91 Kendrick et al., 2012b). Previous studies have highlighted the broad range of

92 geological applications of the halogens as key tracers of petrogenetic processes (Chu

93 et al., 2009; Ladenburger et al., 2016; Teiber et al., 2014; Wang et al., 2014),

94 magmatic degassing (Balcone-Boissard et al., 2010; Collins et al., 2009; Pyle and

95 Mather, 2009), subduction-related metasomatism (Bénard et al., 2016; Bernini et al.,

96 2013; Chavrit et al., 2016; Debret et al., 2016; John et al., 2011; Kendrick et al.,

97 2014a; Köhler et al., 2009; Manzini et al., 2017; Pagé et al., 2016; Straub and Layne,

98 2003), crustal recycling (John et al., 2010; Kendrick et al., 2015), magma source

99 characteristics and mantle melting (Beyer et al., 2016; Joachim et al., 2015; Kendrick

100 et al., 2012a; Roberge et al., 2015; Schilling et al., 1980), the volatile inventory of the

101 subcontinental lithospheric mantle (Broadley et al., 2016), apatite provenance studies

102 (Ansberque et al., 2019), apatite fission track annealing kinetics (Green et al., 1985)

103 and the distribution of magmatic volatiles in the lunar interior (McCubbin et al.,

104 2011). Of societal importance is the role of halogens in the transport and precipitation

105 of ore-forming metals, and thus for exploration of traditional metals and energy

106 critical elements (e.g. Hedenquist and Lowenstern, 1994). The concentrations of

107 halogens and other magmatic volatiles in hydrothermal fluids and gas emissions also

108 constitute valuable tools for monitoring sub-volcanic processes in the magmatic

109 plumbing systems of quiescent and active volcanoes (cf. Aiuppa et al., 2009 for a

110 review).

111

112 *In situ* analysis allows for mineral-specific and even zone-specific measurement of

113 analytes in natural minerals and experimental charges, as well as in crystal-hosted

114 melt and fluid inclusions. A variety of analytical techniques are available for *in situ*

115 halogen determinations including Electron Probe Microanalysis (EPMA)

116 (Ladenburger et al., 2016; McCubbin et al., 2015; Seifert et al., 2000; Zhang et al.,

117 2016), Proton Microprobe (PMP) (O'Reilly and Griffin, 2000), Secondary Ion Mass

118 Spectrometry (SIMS) (Cadoux et al., 2017; Kusebauch et al., 2015b; Kusebauch et al.,

119 2015c; Pagé et al., 2016), Time-of-flight SIMS (TOF-SIMS) (Joachim et al., 2015),

120 Proton Induced X-ray Emission (PIXE) (Bureau et al., 2000; Jochum et al., 2006),

121 Laser Plasma Ionisation Mass Spectrometry (LIMS) (Jochum et al., 2006) and

122 Synchrotron Radiation X-ray Fluorescence (SR-XRF) (Cadoux et al., 2017). Besides

123 EPMA, Laser Ablation Inductively Coupled Plasma Mass Spectrometry (LA-ICP-

124 MS) is a widely available method that has been assessed for the quantification of the

125 halogens (Chew et al., 2014; Fusswinkel et al., 2018; Hammerli et al., 2013; Heinrich

126 et al., 2003; Kendrick et al., 2020; Rottier and Audétat, 2019; Seo et al., 2011). These

127 papers have highlighted the ability of LA-ICP-MS instrumentation to achieve limits

128 of detection of ≈8 µg/g for bromine in scapolite (Hammerli et al., 2013), whilst

129 concentrations ≥500 µg/g are required for chlorine measurements (Chew et al., 2014;

130 Hammerli et al., 2013). Fusswinkel et al. (2018) report a range of detection limits for

131 halogen analysis of fluid inclusions: Cl = 5 – 487 µg/g; Br = 0.4 – 52 µg/g; I = 0.03 –

132 3.64 µg/g. Recent work by Rottier and Audétat (2019) demonstrated that it was

133 possible to analyse glasses containing several hundred µg/g Cl by employing an

134 equation linking the amount of excess Cl to the quantity of aerosol produced to

135 correct for non-sample derived Cl arising from contaminants on the inner surfaces of

136 the sample holder and tubing lines. Using 200 µm diameter laser ablation spots,

137 Kendrick et al. (2020) inferred limits of quantification of ~ 200 µg/g for Cl and ~ 1

138 µg/g for Br in silicate glass (after correction for laser background and REE

139 contributions), and ~ 50 µg/g for Cl and ~ 0.1 µg/g for Br in carbonate. These authors

140 found that iodine can be measured in carbonate and Fe-oxyhydroxide with µg/g I

141 abundances. The sensitivity of halogen analysis in ICP ionisation is limited by their

142 high first ionisation potentials (F = 17.42 eV, Cl = 12.97 eV, Br = 11.81 eV, I = 10.45

143 eV) typically resulting in low sensitivities, while some halogen isotope determinations

144 (e.g. ^{37}Cl, ^{79}Br and ^{81}Br) are also compromised by significant argon-based polyatomic

145 interferences. The ionisation potential of F is higher than that of Ar (15.76 eV), and is

146 therefore impossible to determine by ICP-MS. Notwithstanding, LA-ICP-MS offers a

147 viable alternative to other *in situ* halogen methods based on availability, accessibility,

148 cost and sample preparation requirements compared to the techniques listed above. In

149 addition, electron microprobe analysis of apatite requires careful orientation of the

150 crystallographic c-axis of minerals to avoid halogen migration due to heating effects

151 during analysis (Stock et al., 2015).

152

153 Utilising the results of recent studies designed to establish the halogen contents of

154 readily available glass and mineral reference materials (Balcone-Boissard et al., 2009;

155 Cadoux et al., 2017; Chew et al., 2014; Hammerli et al., 2013; Kendrick et al., 2013;

156 Kusebauch et al., 2015b; Kusebauch et al., 2015c; Marks et al., 2016; Marks et al.,

157 2012; Seo et al., 2011), in this contribution we develop new LA-ICP-MS protocols for

158 rapid (1 min per analysis) Cl, Br and I measurements in a range of geological

159 reference materials, to allow for matrix-matched calibration. Existing data are

160 augmented with new Combustion Ion Chromatography measurements on widely

161 distributed MPI-DING glasses ATHO-G and StHs6/80-G. We assess the impact of

162 ablation parameters including repetition rate, fluence, material hardness and ablation

163 pit aspect ratio to optimise data quality. We also investigate potential gas and matrix-

164 based interferences, along with sample homogeneity, to identify reliable reference

165 materials. We critically evaluate the capability of the technique with an in-depth

166 assessment of accuracy and precision, together with an appraisal of the limits of

167 quantification for a range of ablation spot sizes from 30 – 80 μm. Finally, we present

168 a real-world comparison of LA-ICP-MS Cl data with EPMA determinations on

169 apatite hosted in sub-volcanic lamprophyre from Iberia (Central Spain) and SIMS

170 measurements on glassy quartz-hosted melt inclusions (MI) in rhyolitic deposits from

171 the Okataina Volcanic Centre (Taupo volcanic zone, New Zealand).

172

173 *1.1 Halogens in geological materials*

174 The heavier halogens (Cl, Br and I) are incompatible to highly-incompatible and are

175 typically concentrated in evolved melts and metasomatic fluids and associated

176 volatile-bearing minerals including apatite, scapolite, amphibole and mica. Cl, Br and

177 I are highly soluble in fluid phases (e.g. Bureau et al., 2016; Bureau et al., 2000;

178 Bureau and Métrich, 2003; Cadoux et al., 2018; Kusebauch et al., 2015a), whilst I

179 (and to a lesser extent, Br) are concentrated in organic-rich sediments (Pyle and

180 Mather, 2009), and in some carbonates (John et al., 2011; Kendrick et al., 2020).

181 Crucially, the halogen content of glass and volatile-rich phases can enable the

182 reconstruction of mantle-derived melt compositions, provided appropriate partition

183 coefficients are known. Apatite is a common accessory phosphate mineral in igneous

184 and metamorphic rocks that can accommodate variable amounts of Cl. Igneous apatite

185 is typically fluorapatite with a minor hydroxyl component (<0.2 wt. % Cl; e.g. Teiber

186 et al., 2015); appreciable Cl contents (≥0.5 wt.%) are rare and largely restricted to

187 apatite hosted in mafic rocks such as gabbros (Ladenburger et al., 2016) and highly

188 evolved systems (Webster and Piccoli, 2015). End-member chlorapatite (up to 6.8 wt.

189 % Cl) is commonly associated with the replacement of primary magmatic apatite

190 during metasomatism (e.g. Engvik et al., 2009; Harlov, 2015). Available data indicate

191 that most apatite typically contains <5 µg/g Br (Teiber et al., 2015), however

192 secondary apatite associated with metamorphic/metasomatic overprinting has been

193 found to host up to 85 µg/g Br (Kusebauch et al., 2015b). Scapolite, structural

194 formula $(NaCaK)_4[Al_3(Al,Si)_3Si_6O_{24}](Cl,CO_3,SO_4)$, is dominantly found in

195 metamorphic and metasomatised rocks. The anionic structure of scapolite (corner-

196 sharing Al and Si-tetrahedra that enclose large cavities) allows it to host appreciable

197 quantities of volatile species.

198   Reference glasses are widely used for external standardisation of LA-ICP-MS data, as

199   well serving as secondary standards to monitor accuracy and precision. As discussed

200   by Jochum et al. (2010), published halogen data for geological reference materials are

201   scarce. Notwithstanding, recent work by Marks et al. (2016) reports high-precision

202   values for the complete suite of halogens in USGS synthetic basaltic glasses GSD-1G

203   and GSE-1G determined by the noble gas method. Characterisation of reference

204   materials BHVO-2 and Geological Survey of Japan standards JB-1b and JB-2

205   highlighted that mafic compositions are more reproducible, and therefore better suited

206   for halogen characterisation than more evolved material where variable fractionation

207   may lead to heterogeneous halogen concentrations (Balcone-Boissard et al., 2009).

208   However, concentrations of the halogens are typically higher in more silicic rocks,

209   and so the selection of appropriate natural glasses can be challenging. The increasing

210   availability of fused natural glasses (e.g. MPI-DING glasses) and synthetic doped

211   glasses (e.g. USGS 'GS' series glasses and Corning reference glasses) has served to

212   alleviate these analytical issues, however, the extent and scale of halogen

213   heterogeneity in these materials has not been fully investigated.

214

215   *1.2 Reference materials used in this study*

216   A large number of apatite occurrences have been analysed for Cl contents via LA-

217   ICP-MS and EPMA (Chew et al., 2014), whilst Durango (Mexico) and Ødegården

218   apatite (Norway) have also been characterised for Cl and Br abundances using EPMA

219   and SIMS (Kusebauch et al., 2015b; Marks et al., 2012) as well as CIC and TXRF

220   (Total Reflection X-ray Fluorescence Analysis) techniques (Marks et al., 2012).

221   Teiber et al. (2015) present EPMA Cl data for Otter Lake apatite.

222 In this study, five well known apatite occurrences were selected for analysis; a high

223 purity U-Pb dating standard (Madagascar) and four with crystals large enough to be

224 mounted parallel to the c-axis enabling analysis perpendicular to it (Durango, Otter

225 Lake, Ødegården, 815). The crystals are those characterised previously by Chew et al.

226 (2014), except Madagascar for which multiple fragments of gem roughs were

227 analysed. Chips of the gem quality scapolites BB1, SP and SY were provided by

228 Mark Kendrick. Recommended reference values for Cl, Br and I for the gem scapolite

229 standards have been established using INAA and the NG method (Kendrick et al.,

230 2013), as well as characterisation via LA-ICP-MS (Hammerli et al., 2013). An

231 additional scapolite (meionite) standard NMNH R6600 from Brazil with Cl

232 abundances determined via EPMA (Jarosewich et al., 1980; van der Zwan et al.,

233 2012) was sourced from the Department of Mineral Sciences, Smithsonian Institution.

234 A wide range of silicate glasses were analysed in this study: USGS synthetic basaltic

235 glasses GSC-1G, GSD-1G and GSE-1G; seven MPI-DING glasses spanning a range

236 of major element compositions and Cl contents (Jochum et al., 2006 cf. Table 1); the

237 synthetic archaeological Corning reference glasses A, C and D that have been

238 analysed for Cl contents via EPMA (Adlington, 2017; Vicenzi et al., 2002) and SEM

239 analysis (Kuisma-Kursula, 2000); and the widely distributed NIST Standard

240 Reference Material (SRM) glasses 610 and 612 that have been characterised for Cl

241 and Br mass fractions via LA-ICP-MS (Jochum et al., 2011; Rottier and Audétat,

242 2019; Seo et al., 2011), the noble gas method (Marks et al., 2016) and CIC (Wang et

243 al., 2010). These contributions demonstrate the poor reproducibility of selected

244 halogens in NIST SRM glasses 610 and 612 across a wide range of analytical

245 techniques. As such, these glasses represent ideal reference materials on which to test

246 the nature and origin of spurious positive halogen signals that yield erroneously high

247 concentration values. Detailed background and location information on the origin of

248 all the reference materials listed here are included in Supplementary material file.

249 Published and preferred halogen values (INAA/NG data, agreement across multiple

250 methods/studies and/or dedicated halogen analytical studies) for all the reference

251 materials analysed in this study are summarised in Table 1.

252

253 **2. Methods**

254 2.1 Combustion Ion Chromatography

255 Combustion ion chromatography (CIC) is an automated combination of combustion

256 digestion (pyrohydrolysis) and ion chromatography. We applied combustion ion

257 chromatography at the Fachbereich Geowissenschaften, Tübingen University,

258 Germany. The system comprised a 930 Compact IC Flex chromatograph (Metrohm)

259 with chemical suppression and a peristaltic pump for regeneration (100 mmol/l

260 H_2SO_4), connected to a combustion oven and an autosampler for solid samples (MMS

261 5000; Analytik Jena).

262

263 Aliquots of 50 – 100 mg of the MPI-DING glasses ATHO-G and StHs6/80-G were

264 washed three times in an ultrasonic bath in Milli-Q water and oven dried at 40°C

265 overnight. Reference materials were then powdered using an agate pestle and mortar

266 which was cleaned twice with high purity quartz sand between reference materials.

267 For combustion, a mixture of 10-15 mg of sample powder and the same amount of

268 WO_3 powder (99.995 % - Aldrich 204781) was loaded into a quartz vial that was

269 capped on both sides with quartz wool and placed into glass vessels. The quartz

270 vessels where heated in an extraction line with a constant flow of Ar (grade 6.0; 100

271 ml/min) and O_2 (grade 5.0; 300 ml/min) to 1050°C for 12 min, followed by 10 min of

272 post-combustion and 7 min of cooling. During combustion, a constant water flow (0.2

273 ml/min) was maintained. The loaded steam was collected in an absorbance module

274 containing 4 ml of 0.5 M H_2O_2 solution. After matrix elimination (using a Metrosep A

275 PCC 2 HC/4.0 column) the solutions were injected into the ion chromatograph. We

276 used a Metrosep A Supp 5-250/4.0 (kept at 55°C) and a Metrosep A Supp 4/5/4.0

277 Guard column and an eluent consisting of a mixture of 2mmol NaOH, 1.6 mmol

278 Na_2CO_3, and 5 vol.% acetone at a flow rate of 0.7 ml/min (see Epp et al., 2019 for full

279 details). For quantification of halogen and S concentrations, a primary reference

280 solution was mixed from single element solutions (1000 mg/l; ROTH) and a quadratic

281 6-point-calibration curve that covered the concentrations to be quantified was

282 constructed using the Metrohm intelligent Partial Loop Injection Technique (MiPT).

283 The effective detection limits for powdered samples were about 10–30 μg/g for F and

284 Cl, about 5 μg/g for S, and around 0.3 μg/g for Br. Based on the frequent analyses of

285 standard solutions and various reference materials, relative uncertainties were

286 generally <10% (1σ level) for F and Cl, and up to ~20% for Br and S, depending on

287 the concentrations.

288 2.2 LA-ICP-MS

289 *2.2.1 Sample preparation*

290 Samples were mounted in 25 mm diameter epoxy resin pucks, taking care to orientate

291 crystals with the c-axis parallel to the exposed surface where possible. This mounting

292 procedure was undertaken to avoid halogen migration along the c-axis (cf. Stock et

293 al., 2015) during electron probe microanalysis of apatite, and allows analysis of

294 crystals with a range of techniques. Samples were mounted in Struers® EpoFix two-

295 part resin and were kept at 40°C for 48 hrs prior to polishing on a Struers® LaboPol-

296 21 using 9, 6 and 1 µm diamond suspensions in conjunction with grinding and

297 polishing plates.

298

299 *2.2.2 Instrument setup*

300 Halogen data were acquired using a Teledyne Photon Machines Analyte G2 193 nm

301 Excimer laser ablation system coupled to a Thermo Scientific iCAP Qc ICP-MS at

302 Trinity College Dublin. Ablation was carried out within a HelEx II 2-volume ablation

303 cell and transported to a variable volume signal smoothing device (set at 5 ml) using

304 PEEK (poly ether ether ketone) tubing. The smoothing device was connected to the

305 torch using conventional 3.175 mm ID tubing, providing routine LA system washout

306 times whilst maintaining the PEEK tubing accessory used for ultra-rapid washout

307 mapping applications (not employed here). The carrier gas mixture comprised He

308 (grade 5.0, 99.999% purity; 0.35 ml/min cell, 0.05 ml/min cup) with addition of N_2

309 (13 ml/min) to aid oxide suppression and enhance signal sensitivity and Ar (0.67

310 L/min) for the nebuliser (plasma) gas. Ablation parameters comprise 25 and 50 Hz

311 repetition rates, 2.75 J cm^{-2} laser energy, $30 - 80$ µm square spots, 20 s acquisition

312 time and 40 s washout, the latter portions ($20 - 25$ s) of which were employed for

313 baseline measurements. The selected laser energy represents a compromise in order to

314 achieve suitable ablation characteristics for the range of matrices analysed here.

315 Extended analyte dwell times of up to 250 ms were employed to improve sensitivity

316 and signal stability (e.g. Stead et al., 2017). An analyte list comprising ^{35}Cl, ^{79}Br, ^{81}Br,

317 ^{127}I, ^{208}Pb, ^{55}Mn, ^{29}Si, ^{39}K, ^{23}Na and ^{43}Ca was selected for initial test sessions. A

318 summary of instrument conditions is detailed in Table 2. Instrument tuning was

319 performed using raster scans of NIST SRM 612 (Jochum et al., 2011) at the start of

320 each analytical session. The ICP-MS was tuned to achieve similar sensitivity across

the mass range (Ce, Th and U) whilst maintaining low oxide totals (<0.2 % for

$^{232}Th^{16}O/^{232}Th$) and a Th/U ratio close to unity.

2.2.3 Ablation rate

Inspection of laser pits was carried out to monitor the aspect ratio of ablation volumes and to determine the ablation rate of the range of geological materials analysed in this study. A Filmetrics Profilm3D optical profiler was used to measure pit depths. The instrument was run in vertical scanning interferometry mode and was calibrated at the beginning of each session using the VLSI Standards Inc. Step Height Standard model # SHS − 8.0 QC. For the ablation settings detailed in Table 2, the following average ablation rates were observed: scapolite (0.07 µm/pulse), apatite (0.105 µm/pulse), average silicate glass (0.105 ± 0.05 µm/pulse) and olivine (0.09 µm/pulse). The higher the ablation repetition rate (frequency), the greater the volume of sample material introduced in to the ICP-MS, increasing analyte signal intensity. However, for ablation pits with aspect ratios (depth:width) >1, analyte fractionation increasingly becomes an issue (Woodhead et al., 2004). Accordingly, we suggest lower repetition rates for most applications to preserve a 1:1 crater aspect ratio, and outline a range of ablation parameters (frequency, ablation duration) that maintain these conditions for all materials down to 30 µm spots (Table 4). The fluence employed here (2.75 J/cm^2) provides a uniform rate of signal decay during ablation of all analysed materials. For studies focusing on a single matrix type, the fluence could be optimised further.

2.2.4 Data reduction

Data processing was undertaken using Iolite software v.3 (http://www.iolite.org.au; Paton et al., 2011) run within Igor Pro (http://www.wavemetrics.com). Signal

346   integrations were typically defined for 12 – 14 s, taking care to avoid initial

347   laser/sample coupling and the last 3 s of data acquisition. Baseline time intervals of

348   20 – 25 s were defined manually between each laser firing to acquire local signal

349   minima for all analytes. For a given analytical run, unknowns were calibrated using a

350   single matrix-matched standard in Iolite: scapolites were calibrated using scapolite

351   BB1 (Cl, Br and I); apatites using Durango (Cl) and Ødegården (Br); and reference

352   glasses using NIST SRM 610 (Cl), GSD-1G and GSE-1G (Cl and Br).

353   Determinations on scapolite BB1 and Durango were calibrated using scapolite SY and

354   apatite 815, respectively. Iodine signals for GSE-1G glass were calibrated using BB1

355   scapolite. Although not matrix-matched, a dearth of iodine literature data has hindered

356   routine analytical determinations, and therefore this represents an attempt to constrain

357   the limit of quantification of iodine via LA-ICP-MS. Internal standardisation was

358   carried out using ^{43}Ca (apatite and scapolite) or ^{29}Si (glasses) and the

359   'X_TraceElements_IS' data reduction scheme (DRS) in Iolite. An additional

360   correction was developed for low Cl glasses, where olivine (Cl-free) is bracketed

361   every 2-3 unknowns to account for plasma loading effects as described in section 3.5

362   ('*Blank correction using nominally halogen-free material*').

363

364   2.3 EPMA

365   Apatites hosted in 100 µm-thick polished sections were analysed for P, Ca, F, Cl and

366   S using a JEOL 8600 4-spectrometer electron microprobe at the Research Laboratory

367   for Archaeology and the History of Art, University of Oxford following the approach

368   of Stock et al. (2015). Analyses were acquired using an accelerating voltage of 15

369   keV, a beam current of 10 nA and a 10 µm beam diameter. Peak count times of 120 s

370   were used for Cl and F, 140s for S, 30 s for P and 20 s for Ca. Backgrounds were

371 measured for half the count time either side of the peak. MgF was used as the primary

372 standard for fluorine, and the counts were collected on an LDE crystal, while both Cl

373 and S were analysed on PET crystals. BaFCl was used as the primary standard for Cl

374 and $BaSO_4$ was used for S. The calibration was verified by analysing Durango and

375 Wilberforce apatite crystals that were mounted with their c-axis perpendicular to the

376 beam.

377

378 **3. Results**

379 *3.1. Preliminary tests and analyte selection*

380 In Ar-based plasmas a problematic polyatomic hydride interference ($^{36}Ar^1H^+$) occurs

381 on ^{37}Cl (24.2 % abundance), making ^{35}Cl (75.8 % abundance) the preferred isotope

382 for Cl concentration determinations (Chew et al., 2014; Fietzke et al., 2008). The

383 extent of this interference is apparent in Figure 1a where the background signal on

384 ^{35}Cl is ~4 kcps (thousand counts per second), whereas the ^{37}Cl background is highly

385 variable at ~200 kcps. Thus, ^{35}Cl has significantly higher signal-background ratios

386 compared to ^{37}Cl, and also exhibits more uniform peak shapes and typical ablation

387 signal decay profiles. Bromine has two isotopes ^{79}Br (50.7 % abundance) and ^{81}Br

388 (49.3 % abundance), with background signals for our analytical set-up averaging ~1.7

389 and ~2.6 kcps, respectively (Fig. 1b). During preliminary analytical sessions, both Br

390 isotopes were analysed to investigate their suitability for the range of matrices

391 analysed here, and to provide guidance for characterising and minimising potential

392 interferences. A full appraisal of bromine determinations made using both isotopes is

393 presented in section 3.3, however preliminary bromine results are presented for ^{81}Br

394 in the following section. Iodine has a single isotope (^{127}I) with a background signal of

395 ~10 kcps under normal running conditions (Fig. 2).

396

397 *3.2. Output for Cl, Br and I*

398 *3.2.1. Analytical limits of quantification*

399 The analytical limits of quantification (LOQ) for Cl, Br and I were constrained

400 through a comparison of new uncorrected LA-ICP-MS data with published values

401 determined via NG, SIMS, EPMA, SEM, PIXE, LIMS, CIC, LA-ICP-MS, TXRF and

402 INAA methods (Fig. 2a, see Table 1 for published values). The limit of quantification

403 represents the smallest amount that can be measured with reasonable accuracy, and

404 can be defined as:

405

406 [1] $\text{LOQ } (\mu g/g) = 10 \, s \, / \, m$

407

408 where s represents the standard deviation of y-intercepts for individual LA-ICP-MS

409 analytical sessions, and m represents the average slope of the same regression lines on

410 measured (y-axis) vs. published (x-axis) plots (Harris, 2010). In practice, the LOQ

411 value is rarely reported as it is appreciably higher than the commonly reported limit of

412 detection:

413

414 [2] $\text{LOD } (\mu g/g) = 3 \, s \, / \, m$

415

416 which represents the minimum detectable concentration (too low to measure

417 accurately; Harris, 2010).

418

419 On plots of measured *vs* published values for ^{35}Cl, ^{81}Br and ^{127}I in apatite, scapolite

420 and silicates glasses, materials with appreciable halogen contents ($\geq$700, $\geq$32 and 0.8

421 µg/g, respectively) were used to calculate regression lines. For each isotope, y-

422 intercept values for individual analytical sessions were used to calculate the

423 theoretical limits of quantification according to equation 1, giving the following

424 LOQs for our dataset; Cl = 360 µg/g, Br = 8 µg/g, I = 0.75 µg/g. Calculated LOQs for

425 Cl and Br are of the same order as the LA-ICP-MS limits of detection (LODs)

426 reported by Hammerli et al. (2013) of >500 µg/g and ~ 8 µg/g, respectively. Notably,

427 significant discrepancies exist in the literature regarding the definition of the limit of

428 detection (see Pettke et al., 2012 for a detailed review). For the present study, we use

429 the *limit of detection* of Longerich et al. (1996) taken directly from Iolite, which is

430 most commonly used in the literature and uses data from individual analyses rather

431 than analytical sessions as defined here in equation [2]. Following Longerich et al.

432 (1996), we obtain the following matrix specific average LODs; $^{35}Cl_{glass}$ = 34 µg/g,

433 $^{35}Cl_{apatite+scapolite}$ = 57 µg/g; $^{79}Br_{glasses}$ = 0.6 µg/g, $^{81}Br_{glasses}$ = 1 µg/g, $^{79}Br_{scapolite}$ = 1.2

434 µg/g, $^{81}Br_{scapolite}$ = 1.6 µg/g, $^{79}Br_{apatite}$ = 0.1 µg/g, $^{81}Br_{apatite}$ = 0.15 µg/g; $^{127}I_{all\ materials}$ =

435 0.03 µg/g. However, these limits of detection are deemed unrealistic on account of the

436 overwhelming interference contributions on these isotopes (see section 3.4 onwards).

437 In contrast, the limit of detection formulation of Pettke et al. (2012) (Eq. 6) yields

438 significantly higher values (similar to those provided by LOQ equation [1]), providing

439 a more reliable evaluation of the capability of the technique. Petrus et al. (2017)

440 describe the strengths and limitations of the two main approaches to LOD

441 determinations in LA-ICP-MS analysis (Longerich et al., 1996; Pettke et al., 2012).

442 Both the slopes and R^2 values of regression lines are very close to unity, attesting to

443 the excellent accuracy for the large range of compositions analysed. In all cases,

444 regression lines have significant non-zero y-intercepts (at the 2σ level) suggesting a

445 role for non-sample related contributions to measured signals, even after gas blank

446 correction (Fig. 2a insets).

447

448 In order to better understand the reasons for the non-zero intercepts, we compared raw

449 ICP-MS signal traces in counts per second (cps) for the isotopes ^{35}Cl, ^{81}Br and ^{127}I for

450 a sequence of reference materials comprising scapolites SP, SY, BB1 and silicate

451 glasses NIST SRM 610 and GSD-1G (Fig. 2b). Notably, apparent signals (false

452 signals unrelated to material halogen content) observed in the raw data are present

453 only during laser ablation (absent within background), and most evidently in the case

454 of ^{127}I and ^{81}Br, are not related to the concentration of the analyte in the reference

455 material; at low concentrations (<300 µg/g Cl, ~30 µg/g Br, <0.75 µg/g I), different

456 reference materials return similar LA-ICP-MS results regardless of known

457 concentrations (Fig. 2b). This is the case for reference materials with established Cl,

458 Br and I concentrations below the theoretical limits of quantification. Reference

459 materials containing ≥400 µg/g Cl show excellent agreement between LA-ICP-MS

460 and published data, plotting on the 1:1 line (Fig. 2a). Otter Lake apatite has the

461 lowest Cl concentration of the apatites analysed here and shows a marked deviation

462 from published values; 90 ± 40 µg/g Cl (this study) *vs* 300 – 400 ± 200 µg/g Cl (see

463 Table 1). Notwithstanding the large uncertainty and lack of other low Cl examples,

464 we estimate a limit of quantification of ~500 µg/g Cl for apatite. The glasses selected

465 for this study represent the only analysed reference materials with <300 µg/g Cl. In

466 summary, this set-up is suitable for analysing glasses with >300 µg/g Cl, apatite and

467 scapolite with >500 µg/g Cl and all materials with ≥30 µg/g Br and > 0.75 µg/g I.

468

469 *3.3. Interferences and the origin of apparent signals at low halogen concentrations*

470   In this section, we discuss the origin of apparent signals at low halogen concentrations

471   and develop an approach to correct this effect for chlorine. We define the limit of

472   linearity, which represents the concentration below which LA-ICP-MS chlorine

473   results deviate from the 1:1 line on plots of LA-ICP-MS vs. published values. The

474   limit of linearity is similar to the limit of quantification in that it also represents the

475   smallest amount that can be measured with reasonable accuracy, and here we

476   additionally incorporate a correction for non-analyte related contributions to the

477   measured signal.

478

479   *3.3.1. Instrument resolution; resolving on-mass interferences*

480   The resolution (R) of a mass spectrometer is a measure of its ability to separate ions

481   with small differences in mass. Resolution is defined as $R = m/\Delta m$ where m is the

482   mass of the lighter isotope and Δm the mass difference between the two isotopes of

483   interest. For example, a resolution of 1060 is required to separate ^{35}Cl (34.969 atomic

484   mass units (amu)) *vs* ^{16}O^{18}OH (35.002 amu), whilst a resolution of 5057 is necessary

485   to resolve ^{81}Br (80.916 amu) from ^{40}Ar^{40}ArH (80.932 amu). In normal resolution

486   mode, the iCAP Qc has a resolution of ~125. Although the resolution can be increased

487   by running in high resolution mode (albeit at the expense of sensitivity), it is clearly

488   not possible to separate these isobaric interferences from the target analytes using a

489   single quadrupole instrument. Nevertheless, our set-up provides optimised accuracy

490   and precision for Cl, Br and I analysis by LA-ICP-MS, as discussed below.

491

492   *3.3.2. Collision cell approach*

493   Identical sessions run with and without the use of a collision cell unequivocally

494   demonstrate the contribution of polyatomic species. Runs employing the collision cell

495 were run in collision cell technology sensitivity (CCTS) mode with the collision cell

496 He set at a flow rate of 4 ml/min. Whilst the signal/background ratio for ^{79}Br remains

497 constant with both analytical set-ups, the ^{81}Br signal/background ratio increases when

498 using the collision cell (on account of greater background suppression), confirming

499 the presence of a gas-based interference, likely ^{40}Ar^{40}ArH (Tan and Horlick, 1986).

500 Without the collision cell, elevated ^{79}Br signals for low Br samples ($\leq$ 1 µg/g) show a

501 close correlation with measured K contents (R^2 = 0.98, not shown). Whilst the

502 observed correlation partly reflects interference from ^{40}Ar^{39}K, as suggested by

503 Hammerli et al. (2013), measurement of ^{39}K is itself problematic due to ^{38}ArH, thus

504 the high correlation coefficient may also be the result of argide-based polyatomics.

505 The correlation between measured ^{79}Br and published K concentrations for glasses is

506 poor (R^2 = 0.64, not shown), and is considered an artefact of measurements below the

507 limit of quantification.

508

509 In order to test for S- and Cu-based polyatomic interferences such as ^{34}S^{1}H (^{35}Cl),

510 ^{63}Cu^{16}O (^{79}Br) and ^{65}Cu^{16}O, ^{32}S^{16}O$_3$^{1}H (^{81}Br) (Tan and Horlick, 1986; Vanhoe, 1993),

511 we analysed high-grade (and assumed high purity) sulphide minerals with and without

512 the collision cell. Chalcopyrite-bearing ore was sourced from the Mount Isa inlier,

513 Queensland, Australia. We analysed pyrite from the basal conglomerates of the

514 Mississagi formation, Huronian Supergroup (Canada) where euhedral metamorphic

515 pyrite rims occur as overgrowths on rounded detrital cores (Zhou et al., 2017).

516 Importantly, none of the target analytes show a relative decrease in signal-to-

517 background ratio with the use of the collision cell (not shown), highlighting that S-

518 and Cu-based interferences do not contribute to halogen determinations in our set-up

519 (assuming the collision cell is effective in supressing hydride molecules). The single

520 iodine isotope (^{127}I) shows no clear improvement in the signal/background ratio with

521 the use of the collision cell. Reference materials with variable I contents yield signal

522 intensities with the same order of magnitude for measurements made below the limit

523 of quantification. This observation holds for all materials analysed here, suggesting

524 the presence of a ubiquitous matrix-independent interference on mass 127 (Fig. 2b).

525 In addition, iodine washout times during ablation of scapolites are noticeably longer

526 compared to silicate glasses with comparable iodine contents, highlighting the

527 contrasting behaviour of different matrix materials. Furthermore, it is observed that

528 the mass 127 background is highest (11 − 14 kcps ± 7 % relative) and most variable

529 during sessions where the He cylinder pressure is ≤6000 kPa, suggesting the

530 incorporation of 'heavy' contaminants that accumulate in the basal portion of the

531 cylinder. Potential contaminants include iodine itself, contributing to the observed

532 elevated, variable background. In addition, apparent ^{127}I signals are also higher during

533 low He pressure runs and so we also invoke the presence of polyatomic interferences,

534 potential candidates including ^{126}XeH (Schnetger and Muramatsu, 1996) and ^{111}Cd^{16}O

535 (Bu et al., 2003). Accordingly, the ^{127}I data presented here are limited to analytical

536 session that maintained He pressures >7000 kPa.

537

538 *3.3.3. Mass scan approach*

539 High-resolution mass scans either side of ^{35}Cl (34.969 amu) were performed at 0.05

540 amu increments to assess the potential influence of overlap from adjacent peaks. No

541 signals were resolved on the low mass side between masses 34.5 and 34.8. Similarly,

542 no counts were observed on the high mass side from masses 35.15 to 35.4, beyond

543 which the shoulder of ^{36}Ar is detected. These tests confirm that the interference(s) on

544 ^{35}Cl are not the result of shoulder overlap from neighbouring peaks, instead indicating

545   on-mass interference at the resolution of the ICP-MS. In order to test this hypothesis,

546   ^{35}Cl peak traces for all sample types (glass, apatite, scapolite and olivine) were plotted

547   from masses 34.8 to 35.15 at 0.05 amu increments. Samples show asymmetric peak

548   shapes, with the highest signals consistently falling on the high mass side, a feature

549   confirmed through reflecting the low mass shoulder about the atomic mass of ^{35}Cl at

550   34.969 amu (Fig. 3). The location of the apparent Cl maxima at ~35 amu suggests that

551   the excess signal may be attributed to the presence of $^{16}O^{18}OH$ (35.002 amu),

552    $^{17}O^{17}OH$ (35.006 amu) and $^{17}O^{18}O$ (34.998 amu). The relative abundances of the

553   oxygen isotopes (^{16}O: 99.8 %, ^{17}O: 0.038 %, ^{18}O: 0.2 %) would imply that $^{16}O^{18}OH$

554   and/or $^{17}O^{18}O$ are likely to be the most prevalent polyatomic interferences, and

555   although H_2 is not added in our set-up, the plasma does not operate under high

556   vacuum, and so the presence of atmospheric oxygen and water vapour cannot be

557   excluded. We envisage that such polyatomic interferences become more prevalent

558   under conditions of reduced plasma energy (temperature) related to sample matrix

559   loading (e.g., Fietzke and Frische, 2016; Kroslakova and Günther, 2007), leading to a

560   greater proportion of polyatomic species in the system.

561

562   To further investigate potential interferences on Br isotopes, mass scans were

563   performed at 0.1 amu from 78.5 – 81.5 in order to resolve peak shapes, excepting

564   masses 79.6 – 80.4 to avoid $^{40}Ar^{40}Ar$ (Fig. 4a). Scans from 79 – 79.5 highlight major

565   shoulder overlap from neighbouring peaks on the high mass side for all samples (Fig.

566   4b). The ubiquity of this interference implies that Ar based-interferences are playing a

567   significant role. In detail, the background ICP spectral features obtained by Tan and

568   Horlick (1986) for water and 5 % acid solutions clearly show the asymmetry of the

569    $^{40}Ar^{40}Ar$ peak, with a pronounced tail on the low mass side. The influence of this

570 asymmetry is shown in Figure 4a, where the $^{40}Ar^{40}Ar$ peak can be clearly seen

571 impinging on mass 79. However, not all sample types show a common minimum at

572 mass 79.3, suggesting that Ar-based polyatomic species are not the only source of

573 peak overlap.

574

575 It is apparent from Figure 4b that the asymmetric peak shape on the high mass side of

576 mass 79 is most pronounced for NIST SRM 610, a characteristic replicated to variable

577 extents by most other reference materials, except scapolite BB1. At the resolution of

578 the scans presented in Figure 4b, we are unable to resolve the position of the

579 interfering peak. However, NIST SRM 610 has an elevated Tb concentration (437

580 µg/g), and so we attribute this feature to overlap from both the $^{40}Ar^{40}Ar$ peak and

581 from the $^{159}Tb^{2+}$ peak on ^{79}Br. This inference is consistent with the atomic mass of Tb

582 (158.925 amu), which yields a m/z of 79.463 when doubly charged. Furthermore, Tb

583 is monoisotopic and has a second ionisation energy of 11.52, and so does easily form

584 doubly charged ions. Similarly, $^{158}Gd^{2+}$ and $^{162}Dy^{2+}$ could contribute to elevated Br

585 signals in samples with low Br contents, likely less significantly than $^{159}Tb^{2+}$ on

586 account of their lower relative abundances (see section 3.4). Thus, we propose that the

587 elevated Br content (33 ± 4 µg/g) measured in NIST SRM 610 using ^{79}Br by Seo et al.

588 (2011) is an artefact of peak overlap from $^{159}Tb^{2+}$ (plus $^{158}Gd^{2+}$ and $^{162}Dy^{2+}$) on a low

589 Br signal (NIST SRM 610 Br = 0.24 µg/g by the NG method, Marks et al., 2016).

590 Interference of $^{159}Tb^{2+}$ on ^{79}Br also explains the anomalously high minima measured

591 for GSE-1G at 79.3 amu (Fig. 4b) as a consequence of the elevated Br (285 µg/g) and

592 Tb (480 µg/g) content of this glass. We estimate a Br/Tb ratio for BB1 scapolite of

593 ~400 based on average Gd and Dy concentrations of 1.4 and 0.9 µg/g, respectively

594 (Kendrick et al., 2020) and a Br content of 430 µg/g (Kendrick et al., 2013). The high

595 Br/Tb ratio of scapolite is entirely consistent with the symmetrical peak shape for

596 mass 79 shown by BB1. The signal on [81]Br shows no sign of interference from

597 adjacent peaks for all materials analysed (Fig. 4c).

598

599 The role of matrix effects on halogen measurements via LA-ICP-MS can be assessed

600 through comparison with data obtained using matrix-free techniques including

601 thermal extraction via CIC (Balcone-Boissard et al., 2009; Wang et al., 2010), PH-

602 ICP-MS (Balcone-Boissard et al., 2009) and the NG method (Marks et al., 2016). To

603 evaluate the influence of ^{159}Tb on Br quantification using ^{79}Br, we plotted Br

604 measured/Br published *vs* sample Br/Tb (Fig. 5). Results for reference glasses show

605 that materials with low Br/Tb ratios yield higher measured/published Br values,

606 confirming that Tb content correlates with the excess apparent Br. Our results suggest

607 that peak overlap has a negligible effect for samples with Br/Tb ratios ≥0.6 (Fig. 5),

608 returning measured/published Br values within error of 1 (for materials with Br above

609 the LOQ). In summary, the advantage of lower background on ^{79}Br is negated by the

610 peak overlap from ^{40}Ar^{40}Ar and ^{159}Tb, and the potential for ^{40}Ar^{39}K interference in

611 high K samples. The uniform peak shape and lack of interference from adjacent peaks

612 on ^{81}Br make it our preferred isotope for Br measurements.

613

614 *3.4. Origin of apparent halogen signals*

615 Previous studies have investigated the potential for contamination of volatile elements

616 during laser ablation sampling. Guillong et al. (2008) observed that the excess S

617 intensity during the ablation of quartz increases with crater size, but the magnitude of

618 the S/Si cps ratio decreases with increasing spot size. Similarly, a variety of ablation

619 chamber cleaning procedures were employed by Seo et al. (2011) to reduce excess S

620 (and to a lesser extent Cl and Br) observed during quartz ablation. Apparent analyte

621 signals (and accompanying detection limits) were reduced by cleaning steps, but

622 increased again over several days, implying accumulation. Together, these

623 observations were used to support the inference that the apparent S is not derived

624 from the ablation of quartz itself, but instead from remobilisation within the ablation

625 cell (laser UV radiation) or transport tubing (scrubbing by the particle aerosol).

626 However, the extent of remobilisation is likely strongly system dependent, and so our

627 main aim here is to consider gas-based polyatomic interferences.

628

629 Figure 1a shows raw intensity cps on ^{79}Br and ^{81}Br for GSD-1G glass and Durango

630 apatite. Notably, GSD-1G yields approximately twice the signal intensity on both

631 isotopes relative to Durango, despite the more than two order of magnitude difference

632 in Br content between the two reference materials. This highlights the strong matrix

633 control on analyte signal response. The elevated apparent Br signal in apatite has been

634 shown to originate from the presence of doubly charged Rare Earth Elements (REE)

635 ions such as ^{158}Gd^{2+} (abundance of 24.84%) and ^{162}Dy^{2+} (abundance of 25.5%) on

636 ^{79}Br and ^{81}Br respectively (Fusswinkel et al., 2018), and ^{159}Tb^{2+} on ^{79}Br (this study).

637 These interferences are a product of the typically high REE content of magmatic

638 apatite. Glasses ATHO-G and StHs6/80-G (~1 µg/g Br) show apparent signals on ^{79}Br

639 and ^{81}Br that equate to 3 − 4.5 µg/g Br when calibrated using GSD-1G (32 µg/g Br),

640 consistent with measurements below the calculated theoretical limit of quantification

641 (8 µg/g). The observed lower background counts on ^{79}Br and better signal shape

642 relative to ^{81}Br (for low Br materials) suggests that the apparent signals are the

643 products of relative increases in the proportion of polyatomic gas-based interferences

644 ^{38}Ar^{40}ArH and ^{40}Ar^{40}ArH reaching the detector during ablation, respectively. These

645 observations are consistent with the relative isotopic abundances of ^{38}Ar (0.06 %) and

646 ^{40}Ar (99.6 %).

647

648 *3.5. Blank correction using nominally halogen-free material*

649 In order to investigate the source of false positive halogen signals, picritic olivine

650 from Margi (Cyprus) was used as a halogen-free material (we estimate a nominal Cl

651 value of 0.3 µg/g based on its host basaltic glass Cl content of 260 µg/g (Portnyagin et

652 al., 2002) and $D_{Cl}^{ol/melt} = 0.0012$ (Dalou et al., 2012; Fabbrizio et al., 2013)). Olivine

653 has low REE abundances, so the contribution from doubly charged ^{159}Tb, ^{158}Gd and

654 ^{162}Dy should be minimal. Ablation of olivine clearly shows resolvable signals at mass

655 35 and 79 above background of ~1200 and ~120 cps for a 58 µm spot, respectively

656 (Figs. 3 and 4b). Such signals are only generated during sample ablation and are not

657 present in the background. In order to elucidate the origin of these apparent signals in

658 our set-up, olivine ablations were interspersed every 2-3 unknowns during analytical

659 runs (using identical ablation parameters). Results show that apparent Cl and Br

660 signals increase with increasing spot size (30, 38, 58 µm). However, background

661 corrected ^{35}Cl/^{29}Si, ^{79}Br/^{29}Si and ^{81}Br/^{29}Si cps ratios for olivine remain constant across

662 the range of spot sizes at ~1×10^{-4}, ~1.5×10^{-5} and ~1.35×10^{-5}, respectively (Fig. 6).

663 This highlights that the apparent halogen signals remain proportional to the volume of

664 olivine introduced in to the ICP-MS, demonstrating the role of sample matrix effects

665 (a shift in the sensitivity of an analyte as a function of associated elements and their

666 concentration in the ICP; e.g., Kroslakova and Günther (2007) and references

667 therein). The results depicted in Figure 6 show that, at a given spot size, the

668 halogen/Si ratio varies throughout the duration of a single analytical session, a feature

669 that is more apparent for smaller spots. Indeed, at smaller spot sizes the propagated

670 uncertainties on halogen/Si ratios are appreciably larger, and are inferred to reflect

671 lower measured signal intensities.

672

673 To account for time dependent variation in the contribution of matrix-derived

674 apparent Cl, we developed a modified version of the iolite Data Reduction Scheme

675 (DRS) 'X_Trace_Elements_IS' that defines an excess Cl spline based on apparent Cl

676 signals measured during ablation of nominally halogen-free olivine throughout an

677 analytical run (every 2-3 unknowns). The modified DRS includes a new input field

678 ('Halogen free RM for corr') in the DRS tab which can be used to specify the

679 halogen-free analyses used to calculate the correction factor (the following files are

680 available as electronic Supplementary material: 'X_Trace_Elements_IS.ipf';

681 'IoliteV3Procs.ipf'; supplementary_material.pdf contains detailed instructions on how

682 to use the DRS). Using this DRS effectively performs a second time-dependent

683 correction to all raw cps values (in addition to baseline subtraction) prior to

684 calibration with the external reference material. The Cl correction is most applicable

685 to low Cl materials (< 300 µg/g Cl) as the false signal is proportionally large relative

686 to true Cl. Calibration should be carried out using a reference material with a higher

687 Cl concentration than unknowns. We recommend the use of NIST SRM 610 (390

688 µg/g Cl) for calibration of unknowns with <300 µg/g Cl and GSE-1G (1220 µg/g Cl)

689 for calibration of samples with >300 µg/g Cl. In the following discussion, Cl data and

690 associated accuracy and precision for glasses with <300 µg/g Cl represent corrected

691 values (as determined in this study, Table 3 gives mean values; complete dataset is

692 included in supplementary_data.xlsx). We do not to apply a correction to the Br data

693 given our calculated limit of quantification for Br of ~8 µg/g and the apparent Br

694 signal corresponds to ~1 µg/g. As such, applying a correction to low Br samples (<10

695 μg/g) fails to appreciably improve analytical capability, and the next lowest,

696 independently characterised GSD-1G reference glass has a Br concentration of 32 ± 2

697 μg/g, on which such a correction has a negligible effect. However, a correction would

698 become viable if reference materials with lower Br contents are available for

699 characterisation.

700

701 Although the remobilisation of transport line contamination build-up cannot be ruled

702 out, ablation of a semi-conductor grade silicon wafer using an 80 μm spot rastering at

703 5 μm/s to 'scrub' the lines for 10 minutes failed to produce any discernible reduction

704 in apparent Cl and Br background signals in our set-up. However, we did observe a

705 15-20 % decrease in the ^{127}I baseline, suggesting that additional rigorous cleaning of

706 the sample stage, funnel, tubing lines and torch assembly may help to reduce the ^{127}I

707 background. Indeed, ablation of an iodine salt (RbI) using a 1 μm spot produces a

708 significant I signal that decays over a protracted period of 20 minutes, demonstrating

709 the 'sticky' behaviour of I in the analytical line. Periodic cleaning could be

710 particularly beneficial for systems that routinely ablate large quantities of I-bearing,

711 organic-rich sediments and/or carbonate materials. Whilst we do not test the role of

712 photochemical desorption of halogens from interior surfaces due to laser UV radiation

713 (Guillong et al., 2008; Seo et al., 2011), irradiation tests performed by Rottier and

714 Audétat (2019) failed to replicate an increase in sulphur intensity. Instead, we

715 attribute the elevated Cl and Br signals to an increase in the relative proportion of

716 polyatomic species reaching the detector caused by the reduction in plasma energy

717 due to sample loading during ablation.

718

719 *3.6. Analyte Fractionation*

720 Analytical fractionation results from the variable behaviour of analytes as a function

721 of differences in volatility. Fractionation can occur during time-dependent laser

722 ablation, aerosol transport and ionisation (e.g. Eggins et al., 1998; Horn and Günther,

723 2003; Kroslakova and Günther, 2007). Whilst factors affecting analyte transport (e.g.

724 tubing material/length, sweep gas composition/flow rates) are important

725 considerations, they are largely system dependent and a detailed discussion is beyond

726 the scope of this paper. In order to assess the role, if any, of time-dependent ablation

727 fractionation, we calculated internal standard normalised fractionation index values

728 (FI_{43} normalised to ^{43}Ca) which ratio the first half of the analytical signal to the

729 second half, whilst maintaining an ablation pit aspect ratio of ≤ 1 (Fryer et al., 1995):

730

731 [3]   Fractionation index, $FI_{43} = (I_i/I_{IS})_{first\ half} / (I_i/I_{IS})_{second\ half}$

732

733 Where I_i represents the mean intensity of the analyte mass for the specified time

734 period and I_{IS} represents the intensity of the internal standard, ^{43}Ca, during the first

735 and second half of the ablation. Deviations from 1 indicate time-dependent

736 fractionation. With increasing analyte volatility, no systematic variation in

737 fractionation index is observed; almost all values plotting within 10% of unity, the

738 majority within 5% (Fig. 7). For all SRMs and spot sizes the average FI_{43} is 1.01

739 (range 0.92 – 1.12), suggesting time-dependent fractionation is minimal for our

740 analytical set-up.

741

742 *3.7. Ionisation*

743 Ionisation conditions within the plasma are strongly controlled by torch position,

744 nebuliser gas flow and radio frequency (RF) power, careful optimisation of which

745 ensure high sensitivity. The introduction of sample aerosol during ablation results in

746 loading of the plasma and a reduction in plasma temperature. This, in turn, leads to a

747 reduction in ionisation efficiency and a relative increase in the proportion of

748 polyatomic species. This theory agrees with the observation that excess apparent Cl,

749 Br and I signals only occur during sample ablation, and although UV scattering

750 effects cannot be ruled out, constant halogen/internal standard ratios across a range of

751 spot sizes (Fig. 6) support a significant role for polyatomic interferences resulting

752 from matrix loading of the plasma. Increased oxide production may also, in part, be

753 due to additional oxygen introduced from the sample matrix itself, but this remains

754 very difficult to quantify. However, such effects are also expected for calibration

755 standards and our analytical set-up is optimised for minimal oxide formation during

756 ablation. As discussed previously, ^{79}Br has been shown to suffer from an argon-based

757 peak shoulder overlap ($^{40}Ar^{40}Ar$) and a matrix-based interference ($^{159}Tb^{2+}$) for

758 samples with Br/Tb <0.6.

759

760 **4. Discussion**

761 *4.1. Accuracy and precision*

762 Figure 8 shows plots of analytical bias (accuracy) *vs* relative standard deviations (2

763 RSD = precision) for Cl and Br in analysed reference materials using 58 μm square

764 spots from a minimum of *n*=10 analyses. For Cl determinations, the majority of

765 reference materials analysed yielded bias and 2 RSD values of ≤10 % (Fig. 8a). Glass

766 BCR2-G (Cl = 67 μg/g) returns a respectable 2 RSD value of ~10 %, however

767 accuracy relative to bulk technique results is poor. Conversely, NIST SRM 612,

768 ML3B-G and KL2-G have good to excellent accuracy but poor reproducibility.

769 Glasses BHVO2-G, ATHO-G, StHs6/80-G, T1-G, GOR128-G and apatite Otter Lake

770   all show significantly elevated bias in accuracy and 2 RSD values, suggesting

771   chlorine heterogeneity at the scale of >58 μm. Ødegården apatite shows excellent

772   accuracy (0.1 %), however a 2 RSD value of 8.6 % combined with the high Cl content

773   of this end-member chlorapatite has the potential to produce increased errors on the

774   calibration of more common low-Cl fluorapatites. 815 apatite represents an ideal

775   calibration standard with bias and 2 RSD values of <5 %. In house Durango and

776   Smithsonian NMNH 104021 Durango apatite yielded comparable reproducibility (2

777   RSD values of 8.6 % and 7 %, respectively), however the improved accuracy (1.6 %

778   *vs* 8.4 % relative error, respectively) of the in house Durango likely reflects analysis

779   of a single crystal slab, rather than the small (150 – 250 μm) crystal fragments of

780   NMNH 104021 Durango. All scapolites characterised in this study represent excellent

781   reference materials for Cl measurements, with 2 RSD and bias values of ≤6 % and

782   ≤2.7 %, respectively. Scapolite SY offers the greatest accuracy and SP the best overall

783   combination of accuracy and precision (Fig. 8a). In terms of glasses, both GSE-1G

784   and NIST SRM 610 represent optimal calibration materials with 2 RSD and bias

785   values of ≤9 % and ≤3 % respectively. As discussed previously, the higher Cl content

786   of GSE-1G (1220 μg/g) is well suited for calibration of glasses with >300 μg/g Cl,

787   whereas NIST SRM 610 is recommended for standardisation of low Cl (<300 μg/g)

788   glasses. Smithsonian Corning glasses A, C and D have 2 RSD values of 6.5 – 9.5 %

789   and accuracies of ≤1.6 %, making them reliable reference glasses for intermediate to

790   high Cl applications. Of the low Cl glasses, GSD-1G yielded bias and 2 RSD values

791   of ~ 11.3 % and 2.8 % respectively, making it a suitable secondary reference standard

792   for analytical sessions involving low Cl (≤ 150 μg/g) glasses.

793

794 Replicate analysis of Br in GSE-1G and GSD-1G confirm that these glasses provide

795 suitable calibration and quality monitor standards with 2 RSD of 9 and 10.5 %

796 respectively, with deviations in accuracy of ≤1.4 % (Fig. 8b). GSE-1G (285 µg/g) is

797 appropriate for high Br (100s µg/g) unknowns whilst GSD-1G (32 µg/g) is best suited

798 to low-intermediate Br measurements (10s µg/g). Results for scapolite SY provide the

799 best accuracy (3.9 %), with BB1 and SP yielding values of 6.2 % and 6.5 %,

800 respectively. All three gem scapolites return 2 RSD values of ≤6.5 % for Br

801 determinations (Fig. 8b).

802

803 Once corrected using nominally halogen-free olivine, a limit of linearity of ~ 100 µg/g

804 is achieved for Cl in glasses, a value that is well defined due to the abundance of

805 reference glasses with Cl mass fractions of 50 − 150 µg/g (Fig. 9a). For reference

806 materials with >30 µg/g Br, LA-ICP-MS data are in close agreement with published

807 values (Fig. 9b). The very clear disparity shown by NIST SRM 610 can be explained

808 by the low Br/Tb of this glass (Fig. 5). However, the scarcity of well characterised,

809 homogeneous reference materials in the 5 − 20 µg/g Br range hinders our ability to

810 test the theoretical LOQ for Br (8 µg/g). However Cadoux et al. (2017) produced well

811 characterised intermediate and evolved glasses with a useful 10 µg/g Br and high

812 Br/Tb ratios. Although not analysed here, we encourage the analysis of these glasses

813 to test the LOQ for Br using LA-ICP-MS. The low Br/Tb of low Br glasses analysed

814 here impedes an accurate assessment of the limit of linearity, however we estimate it

815 to be ~ 2 µg/g (Fig. 9b) and could be defined with greater precision with a larger

816 number of well characterised reference materials. Importantly however, Kendrick et

817 al. (2020) provide a working doubly charged REE correction that effectively lowers

818   the Br LOQ in silicate glass to ~ 1 µg/g, demonstrating the potential of LA-ICP-MS

819   for the measurement of Br in volcanic glasses.

820

821   *4.2. Ablation spot size/area*

822   The effect of spot size/area on the analytical limit of quantification for Cl and Br was

823   assessed using a range of square spots from 30 – 80 µm (Figs. 10 and 11). For

824   chlorine, gem-quality scapolites return excellent accuracy and reproducibility across

825   all spot sizes (Fig 10a). Smithsonian scapolite R6600 consistently returns higher Cl

826   contents than the results of van der Zwan et al. (2012), with our data showing closer

827   agreement with the measurements of Jarosewich et al. (1980). Of the apatites analysed

828   here, Durango and 815 represent ideal reference standards for all spot sizes.

829   Madagascar shows inferior accuracy (bias = 12.6 %) relative to other apatites,

830   however the data are reproducible at variable spot sizes. The elevated bias values for

831   Madagascar likely reflect sample heterogeneity across the multiple gem roughs

832   analysed here, as well as the lowest Cl contents above the limit of linearity.

833   Accordingly, as for Durango, it is advisable to analyse a single, independently

834   characterised crystal fragment, to ensure reproducibility of results. In the case of

835   glasses, occurrences with intermediate Cl values (200 – 2000 µg/g) plot well within

836   error of published values for all spot sizes, with the exception of ATHO-G (Fig 10b).

837   Glass GSD-1G provides the most consistent results across all spot sizes and is our

838   preferred low-Cl glass reference material. Low-Cl (~50 µg/g, Fig. 10c) glasses show

839   high uncertainties (32 – 39 % 2 RSD), indicating that these concentrations are close to

840   the limit of detection of the technique and are in good agreement with the average of

841   calculated LOD values for glasses from Iolite (34 µg/g using Longerich et al., 1996).

842

843   For bromine, determinations for scapolites SY and SP are comparable for spots of 30

844   – 80 µm, plotting at the upper bounds of their respective published data ranges (Fig.

845   11a and b). In contrast, scapolite BB1 also yields similar Br values, but at the lower

846   end of the known field (Fig. 11a). Glasses GSE-1G and GSD-1G yield data within

847   error of the published range, however averages at 30 and 38 µm plot at the lower

848   limits. For all reference materials, ^{81}Br determinations show closer agreement with

849   known values, a feature that is most pronounced for glasses measured using larger

850   spot sizes (58 and 80 µm).

851

852   As discussed previously, Figure 1 shows clear evidence for the impingement of the

853   low mass tail of ^{40}Ar^{40}Ar on ^{79}Br, whilst Figure 7 supports the theory that the

854   magnitude of the excess positive Br signal scales with sample matrix input.

855   Accordingly, the improved accuracy of ^{81}Br measurements relative to ^{79}Br,

856   particularly at larger spot sizes, is inferred to reflect an increase in the extent of

857   ^{40}Ar^{40}Ar peak broadening (Fig. 4a) as a result of reduced ionisation efficiency of the

858   plasma. Additionally, matrices with high REE contents (apatite, NIST SRM 610,

859   GSE-1G) introduce polyatomic interferences through doubly charged cations (^{158}Gd^{2+}

860   and ^{159}Tb^{2+} on ^{79}Br; ^{162}Dy^{2+} on ^{81}Br).

861

862   *4.3. Reference material homogeneity*

863   In reference glasses, there is a general tendency for measured Cl concentrations to

864   deviate from accepted values at smaller spot sizes. At 30 and 38 µm, Corning glasses

865   and GSE-1G return slightly higher values, and NIST SRM glasses and GSD-1G

866   lower, relative to measurements with larger spots (58 and 80 µm). Such deviations

867   suggest sample heterogeneity at a scale smaller than the ablation spot size (Fig. 10b),

868 however all data plot within 2s error of published values. Nevertheless, for glasses

869 with ≥400 µg/g Cl, results show excellent agreement with independent data down to

870 30 µm spots. For all spot sizes, ATHO-G yielded elevated Cl contents relative to CIC

871 values (Fig. 10b), suggesting large scale heterogeneity in this glass. Similarly,

872 StHs6/80-G and T1-G plot at the upper limit of bulk technique results, with NIST

873 SRM 612 consistently returning low results, implying the *in-situ* method samples

874 localised heterogeneities in these glasses (Fig. 10c). Despite large uncertainties,

875 results for Hawaiian glasses KL2-G and ML3B show excellent accuracy (0.6 and 3.1

876 %, respectively) indicating that these glasses may constitute homogenous reference

877 materials suitable for in-situ techniques with higher sensitivity than LA-ICP-MS (e.g.

878 SIMS).

879

880 Published Cl data for the Smithsonian Corning glasses (Adlington, 2017; Kuisma-

881 Kursula, 2000; Vicenzi et al., 2002) show significant deviation from nominal values

882 based on precursory powder mixtures reported by Brill (1972), Table 1. Our data

883 show excellent agreement with published glass determinations, with relative errors of

884 <1.6 % and 2 RSDs of <10 % (Fig. 8a). We concur with previous studies proposing

885 that lower measured glass values (Cl for Corning A = 914 µg/g, C = 690 µg/g, D =

886 1610 µg/g; this study) relative to nominal compositions (Corning A = 1000 µg/g, C =

887 1000 µg/g, D = 4000 µg/g; Vicenzi et al., 2002) likely reflect volatile loss during

888 fusion, with the degree of retention a function of individual glass compositions

889 (Adlington, 2017). Notably, Corning glass C yields low Cl contents (700 µg/g) when

890 analysed with larger beam/spot sizes of 30 µm (Kuisma-Kursula, 2000), 40 µm

891 (Vicenzi et al., 2002) and 58 µm (this study). In contrast, using a beam diameter of 10

892 µm results in a measured Cl concentration of 1300 ± 500 µg/g (Kuisma-Kursula,

893   2000). We interpret these results to reflect small scale (~10 μm) heterogeneity with

894   highly variable Cl contents that produces low 'averaged' Cl mass fractions at larger

895   beam/spot sizes.

896

897   For Br analyses using spots between 30 − 80 μm, all scapolite occurrences give 2

898   RSD of 5 − 10 %, with higher values for the low Br scapolite SP (Fig. 8b). USGS

899   glasses GSE-1G and GSD-1G returned 2 RSD of ≤10 % for 58 and 80 μm spots,

900   increasing to ~13 % for 38 μm spots. GSE-1G gave a 2 RSD of 16 % at 30 μm, whilst

901   a value of 23 % for GSD-1G may, in part, reflect small-scale heterogeneity.

902

903   4.4 Advancements in LA-ICP-MS halogen analysis

904   Here we employ a relatively short data integration period (12-14 s) using a high

905   ablation repetition rate (25 Hz) to achieve a high sample throughput, and by inference,

906   high signal intensity. Signal stability is enhanced for all matrices through the use of

907   extended analyte dwell times (up to 250 ms). Scanning interferometry provides

908   valuable constraints on matrix specific ablation rates that can be used to estimate

909   ablation pit depth and effectively monitor time-dependent elemental fractionation.

910   High resolution mass scans can be used to identify on mass polyatomic interferences

911   (e.g. oxides on ^{35}Cl) and the influence of overlap from neighbouring peaks (e.g.

912   ^{40}Ar^{40}Ar and ^{159}Tb^{2+} on ^{79}Br). We advocate this approach as an effective method for

913   identifying the origin of false positive signals in well characterised reference

914   materials. Once established, it is possible to develop protocols for reducing the limit

915   of linearity, as demonstrated here for low Cl glasses (~100 μg/g Cl). Improvements in

916   the accuracy and precision of halogen measurements using LA-ICP-MS are strongly

917 dependent on the availability of matrix matched reference materials, particularly at

918 low concentrations.

919

920 **5. Recommendations**

921 We advise the use of ^{35}Cl and ^{81}Br isotopes for halogen determinations via LA-ICP-

922 MS. Chlorine measurements using LA-ICP-MS have a limit of linearity of ~ 100 µg/g

923 for silicate glass and an LOQ of ~500 µg/g for apatite. The isotope ^{79}Br experiences

924 significant peak impingement from the low mass shoulder of the ubiquitous ^{40}Ar^{40}Ar

925 peak and the strongly overlapping ^{159}Tb^{2+} peak (m/z = 79.463) in materials with

926 Br/Tb <0.6. The current paucity of homogeneous low Br reference materials with

927 Br/Tb >0.6 limits the usefulness of the potential increased sensitivity provided by the

928 collision cell. The single isotope of iodine (^{127}I) returns a limit of quantification of

929 0.75 µg/g for all analysed materials using He cylinder pressures >7000 kPa.

930

931 Instrument parameters (spot size, repetition rate, ablation duration) should be

932 optimised to maximise signal intensity whilst maintaining an ablation crater aspect

933 ratio (depth:width) of <1:1. Routine duty cycles of <650 ms can be achieved by

934 selecting a restricted range of target analytes and appropriate internal standard(s) (e.g.,

935 ^{43}Ca or ^{29}Si), whilst extending halogen dwell times (^{35}Cl = 100 ms, ^{81}Br, ^{127}I = 250

936 ms).

937

938 The three-gem quality scapolites analysed here represent excellent reference materials

939 for the standardisation of intermediate to high Cl and Br scapolites. Smithsonian

940 meionite R6600 is also ideal, and here we provide the first published Br value for this

941 readily available scapolite. Once independently characterised, Ødegården apatite

942 represents an ideal calibration standard for chlorapatite, however it should be used

943 with caution for standardisation of low-Cl fluorapatites. We recommend that

944 individual crystals of all apatites, particularly Durango, Ødegården and Madagascar

945 analysed here, should be first characterised using EPMA or SEM techniques to

946 account for inter-crystal heterogeneity, using as low a beam current as possible to

947 minimise halogen migration (e.g., Ansberque et al., 2019; Stock et al., 2015). GSE-1G

948 and Corning glasses A, C and D are suitable for the calibration of intermediate to high

949 Cl content glasses (>300 µg/g). For calibration of low Cl glasses (<300 µg/g), NIST

950 SRM 610 is well suited, with GSD-1G as a secondary reference material. Despite

951 having Cl contents approaching the limit of detection for LA-ICP-MS, Hawaiian

952 glasses KL2-G and ML3B-G appear to be relatively homogeneous and suitable for

953 low-level Cl standardisation. With the low Br, low Br/Tb glasses analysed here we are

954 unable to test the theoretical calculated LOQ of 8 µg/g for Br, however we infer a

955 limit of linearity of ~2 µg/g for silicate glasses (Fig. 9b). The observed disparity in

956 analytical signal response shown by different matrices (Figs. 1b and 2b, and persisting

957 even after internal standard correction), highlights the importance of matrix matched

958 calibration and the identification of matrix dependent interferences.

959

960 The limit of linearity for Cl in low Cl glasses is demonstrated to be ~100 µg/g (down

961 from 360 µg/g) through the subtraction of time-dependent apparent Cl signal

962 contributions resulting from oxygen-based polyatomic interferences. As such

963 contributions are only observed during sample ablation, the regular baseline

964 subtraction fails to correct for these analytical artefacts. Accordingly, we advocate a

965 second normalisation of raw cps ^{35}Cl data prior to calibration in order to account for

966 on mass polyatomic oxide interferences. We provide our 'nominally halogen-free'

967 method as an Iolite-based, time-dependent spline correction implemented through an

968 updated version of the 'X_Trace_Elements_IS' data reduction scheme (available as

969 electronic Supplementary material). The correction utilises apparent Cl measured in

970 halogen-free olivine to quantify and remove the portion of the raw signal originating

971 from an increase in the proportion of polyatomic oxides reaching the detector due to

972 plasma loading during sample introduction. In line with this approach, Petrus et al.

973 (2017) propose that true LODs should be calculated from a real ablation blank (rather

974 than a gas blank), by producing data from a material that is completely devoid of the

975 target analytes. For the utility of off-line data corrections (e.g. a doubly charged REE

976 correction on Br (Kendrick et al., 2020)), we recommend establishing instrument- and

977 session-specific equations based on the measurement of reference materials with

978 matching matrices and similar major and interfering element profiles.

979

980 **6. Case studies**

981 *6.1 Apatite in sub-volcanic lamprophyre*

982 Rim to rim Cl transects were acquired across the widths of large (2 – 5 mm length)

983 apatite grains in sub-volcanic lamprophyre Pan-57 (Galé Bornao, 2005) associated

984 with an Early Permian magmatic event in the Iberian Chain, Central Spain (Lago et

985 al., 2004). Profiles across the widths of seven large acicular apatite crystals were

986 measured to ensure the electron beam remained perpendicular to the c-axis during

987 data acquisition. The number of data points ranged from 10 – 20 depending on crystal

988 size. EPMA profiles were replicated via LA-ICP-MS analysis using 30, 38 and 58 μm

989 square spots. Laser transects were oriented parallel to EPMA profiles at a distance of

990 100 – 150 μm and the results are presented in Figure 12. In-house secondary

991 standards Durango apatite and Wilberforce apatite (Ontario, Canada) were run

992 periodically as data quality monitors. Electron microprobe measurements of Durango

993 (n = 4) and Wilberforce (n = 5) apatites (Table 3) show excellent agreement with

994 published EPMA data with relative errors on F of 2.2 and 0.8 % and 2 RSDs of 2.5

995 and 1.6 %, respectively based on values from Sarafian et al. (2013). The Cl mass

996 fraction in Wilberforce was below the limit of detection and Durango yielded a

997 relative error of 7.4 % and 2 RSD of 11.4 % using the average Cl content from

998 (Kusebauch et al., 2015c, Table 1). Overall, the lamprophyre apatite LA-ICP-MS data

999 agree within 0.5 – 7.3 % of the electron microprobe results. As shown in Figure 12,

1000 the greatest disparity is observed for 58 μm laser spots (2.2 – 7.3 % bias), indicating

1001 that the scale of Cl heterogeneity in the apatites is present at a smaller scale. Close

1002 agreement between the two methods is apparent at 30 and 38 μm laser spots (0.5 – 0.9

1003 % bias), suggesting that Cl is homogeneously distributed within the apatite grains at

1004 the 10 – 40 μm scale. Despite the increased uncertainty associated with the 30 μm

1005 analyses, attributed to reduced signal intensity, accuracy remains better than 1 %

1006 relative.

1007

1008 *6.2 Quartz-hosted melt inclusions*

1009 Chlorine concentrations were measured in quartz-hosted melt inclusions (MI) in

1010 rhyolitic deposits from the Okataina Volcanic Centre, Taupo volcanic zone, New

1011 Zealand. Inclusions were targeted in two samples; sample 559 which represents

1012 juvenile material from a massive, poorly sorted pyroclastic flow from the ~50 ka

1013 Rotoiti caldera forming eruption (Shane et al., 2005) and sample 853, a crystal-rich

1014 pumice clast from the Earthquake Flat Pyroclastic eruption that immediately followed

1015 the Rotoiti event from vents located 20km to the SW of the Rotoiti caldera rim

1016 (Molloy et al., 2008). All MI are silicic in composition (72.26 – 76.22 % m/m SiO_2,

1017   Smith et al., 2010), dominantly round to oblate, with no evidence for recrystallisation.

1018   The largest inclusions (~50 µm) were targeted for analysis. Quartz-hosted MI were

1019   previously analysed for Cl using SIMS and were found to contain 263 – 500 µg/g Cl

1020   (Smith et al., 2010). LA-ICP-MS Cl determinations were made on the same samples

1021   (but not necessarily on the same inclusions) using 40 µm square spots (or 80*20 µm

1022   rectangular slits), a 25 Hz repetition rate and 24 s data acquisition (600 shots). The

1023   isotopes ^{35}Cl, ^{81}Br, ^{43}Ca and ^{29}Si were measured. Integrations taking in only MIs were

1024   selected by monitoring ^{29}Si, which was also used as the internal elemental standard on

1025   account of the low Ca contents. NIST SRM 610 was used as the calibration reference

1026   material and data reduced using Iolite v.3. Replicates of homogeneous low-Cl

1027   reference glasses (this study, n = 2) run as unknowns during a one-hour analytical

1028   session gave the following relative errors (%): NIST SRM 612 (11.8), GSD-1G (8.9),

1029   ML3B-G (5.9) and KL2-G (5.9) (halogen-free corrected). ^{81}Br measurements on all

1030   MI were below the limit of quantification and are not considered in the following

1031   discussion.

1032

1033   A total of nine inclusions were analysed (one ablation spot per inclusion); five in

1034   sample 559 and four in sample 853. Sample 559 yielded two populations; two

1035   inclusions with 260 ± 70 and 248 ± 64 µg/g Cl (apparent concentrations of 590 ± 60

1036   and 598 ± 74 µg/g Cl, respectively, prior to halogen-free correction), and three

1037   inclusions with 1740 – 1960 µg/g Cl. Sample 853 returned a single population with a

1038   Cl range of 1690 – 1920 µg/g. The low Cl inclusions in sample 559 show excellent

1039   agreement with the SIMS data of Smith et al. (2010), while the higher values

1040   observed in both 559 and EQF (853) are consistent with electron microprobe matrix

1041   glass compositions (Shane et al., 2005), and clearly demonstrate the reduction in the

1042 analytical limit of quantification offered by the halogen-free correction. Additionally,

1043 our new data extend the range of Cl contents in MI hosted in both the Rotoiti and

1044 EQF eruption deposits from Okataina. All new data acquired in this study on case

1045 study samples are included in file supplementary_data.xlsx.

1046

1047 **7. Conclusions**

1048 Cl, Br and I can be measured reliably in geological materials via matrix-matched LA-

1049 ICP-MS analysis, without the need for pre-irradiation to remove surface-bound

1050 halogens. LA-ICP-MS provides an accessible, rapid technique (1 min per analysis)

1051 with minimal sample preparation and straightforward offline data reduction. It offers a

1052 high sensitivity/cost ratio for Cl, Br and I, variable sampling resolution, selection of a

1053 time resolved signal and minimisation of analyte volatility effects. Through the

1054 implementation of corrections for false ablation derived signal contributions, the limit

1055 of linearity in silicate glass is ~100 µg/g for ^{35}Cl. We propose an estimate of ~2 µg/g

1056 for the limit of linearity of Br in glass. Using a large spot size (200 µm), Kendrick et

1057 al. (2020) suggested limits of quantification of ~200 µg/g Cl and ~1 µg/g Br in

1058 glasses after removal of laser backgrounds and correction of REE contributions.

1059 These results demonstrate the utility of LA-ICP-MS as an appropriate technique for

1060 the determination of Cl and Br in volcanic glasses. In addition, we infer a limit of

1061 quantification of 0.75 µg/g for ^{127}I in all materials characterised here. This allows LA-

1062 ICP-MS I measurements in a variety of iodine rich minerals including scapolite,

1063 carbonates and clays. The mineral phases scapolite and apatite typically contain

1064 appreciably higher Cl mass fractions, and for the latter we estimate a limit of

1065 quantification of ~500 µg/g. These capabilities are maintained for square ablation

1066 spots down to 38 µm (1444 µm^2) for Cl and 30 µm (900 µm^2) for Br. Accuracy and

1067 precision improve with increasing spot size and remain below 6.4 % and 12.9 %,

1068 respectively, for Cl in individual apatite crystals during matrix-matched analysis

1069 down to 30 μm square spots. Under the same conditions, analyses of scapolite return

1070 accuracy and precision better than 4.5 % and 7.1 % for Cl and 11.5 % and 10.3 % for

1071 Br. Low Cl silicate glasses (< 300 µg/g Cl) are most affected by the presence of

1072 isobaric oxide interferences on ^{35}Cl. Accordingly, we provide a time-dependent spline

1073 correction implemented through an updated Iolite software data reduction scheme

1074 ('X_Trace_Elements_IS') in conjunction with a new DRS input field ('Halogen free

1075 RM for corr') to define the nominally volatile free analyses used to calculate the

1076 correction factor. Attempts to define limits of linearity for Br and I using a similar

1077 approach are hindered by: (1) the scarcity of SRMs with well characterised Br

1078 contents in the range 1- 20 µg/g with Br/Tb >0.6 (we estimate it to be ~ 2 µg/g,

1079 although the glasses produced by Cadoux et al., 2017 may help to alleviate this issue);

1080 and (2) the magnitude of interference derived contribution(s) to the measured ^{127}I

1081 signal.

1082

1097

Figure Captions

1099   Figure 1 Raw intensity counts per second (cps) signal traces for (a) ^{35}Cl and ^{37}Cl for

1100   Durango, Tioga and Ødegården apatites. Note that Tioga was only measured in

1101   preliminary test runs and not fully characterised for halogen contents in this study. (b)

1102 ^{79}Br and ^{81}Br for GSD-1G glass and Durango apatite and (c) glasses GSD-1G,

1103   ATHO-G and StHs6/80-G. Significantly, GSD-1G yields approximately twice the

1104   signal intensity on both isotopes relative to Durango, despite the more than two order

1105   of magnitude difference in Br content between the two reference materials,

1106   highlighting the strong matrix control on analytical signal response and the necessity

1107   of matrix-matched calibration. The anomalously high Br signal measured in Durango

1108   is considered to reflect the presence of ^{158}Gd^{2+}, ^{159}Tb^{2+} and ^{162}Dy^{2+} in REE rich

1109   apatite. ATHO-G and StHs6/80-G glasses (~1 µg/g Br) show apparent signals on ^{79}Br

1110   and ^{81}Br that equate to 3 − 4.5 µg/g Br, suggesting measurements made below the

1111   limit of detection. The uniform peak shape of ^{81}Br and reduced interferences make it

1112   our preferred isotope for Br measurements (see text for a detailed discussion).

1113

1114   Figure 2. (a) Plots of measured *vs* published values for the isotopes ^{35}Cl, ^{81}Br and ^{127}I

1115   in apatite, scapolite and silicate reference glasses used in this study. Black symbols

1116   denote materials with appreciable halogen contents used to define the regression lines

1117   (orange dotted lines). All data represent mean values across multiple analytical

1118   sessions. Insets highlight non-zero Y-intercept values for all three isotopes. Grey

1119   symbols denote reference materials excluded from the regression equations and below

1120   the theoretical limits of quantification (LOQ). LOQ calculations (Eq. 1: 10 s / m;

1121   Harris, 2010) are shown for each isotope with s values (standard deviation of y-

1122   intercepts for individual LA-ICP-MS analytical sessions) and m values (average slope

1123   of regression lines on measured (y-axis) vs. published (x-axis) plots) representing data

1124   from individual sessions (not shown). Apatites were explicitly excluded from the Br

1125   LOQ calculation due to a lack of published values for calibration and comparison

1126   purposes. (b) Uncorrected raw ICP-MS signal traces (cps) for the isotopes ^{35}Cl, ^{81}Br

1127   and ^{127}I for scapolites SP, SY, BB1 and glasses NIST SRM 610 and GSD-1G.

1128   Apparent signals are present only during laser ablation (absent within background),

1129   and most clearly in the case of ^{127}I and ^{81}Br, are not related to the concentration of the

1130   analyte in the reference material. The elevated Dy content of NIST SRM 610 (437

1131   µg/g) relative to GSD-1G (51.2 µg/g) contributes to the anomalously high apparent

1132 ^{81}Br signal measured in the NIST SRM glass due to ^{162}Dy^{2+}.

1133

1134   Figure 3. High-resolution peak scans of ^{35}Cl (amu = 34.969) at 0.05 amu increments

1135   for spot analyses of reference glasses, Durango apatite, BB1 scapolite and Cypriot

1136   olivine. Mass scans show that ^{35}Cl is not affected by overlap from neighbouring

1137   peaks, instead indicating on-mass interference(s). All analysed materials show

1138   asymmetric peak shapes, with the highest signals falling on the high mass side, a

1139   feature confirmed through reflection of the low mass shoulder about the ^{35}Cl amu

1140   value of 34.969 (dashed lines). The location of the apparent Cl maxima at ~35 amu

1141 suggests that the excess signal may be attributed to the presence of $^{16}O^{18}OH$ (35.002

1142 amu), $^{17}O^{17}OH$ (35.006 amu) and $^{17}O^{18}O$ (34.998 amu).

1143

1144 Figure 4. (a) Background ICP spectra taken from Tan and Horlick (1986) for water

1145 and 5 % acid solutions clearly show the asymmetry of the $^{40}Ar^{40}Ar$ peak, with a

1146 pronounced tail on the low mass shoulder that visibly impinges on mass 79. (b) and

1147 (c) Raw intensity counts per second (cps) for mass scans from 78.5 − 81.5 atomic

1148 mass units (amu) at 0.1 amu increments to resolve measured peak shapes (excepting

1149 masses 79.6 − 80.4 to avoid $^{40}Ar^{40}Ar$ at 79.925 amu). Scans from 79 − 79.5 highlight

1150 major shoulder overlap from neighbouring peaks on the high mass side for all samples

1151 (except scapolite BB1). The high estimated Br/Tb ratio of scapolite (~400) is entirely

1152 consistent with the symmetrical peak shape at mass 79 shown by BB1. A lack of

1153 overlap on the ^{81}Br signal demonstrates an absence of interferences from adjacent

1154 peaks.

1155

1156 Figure 5. Plot of Br measured/Br published vs Br/Tb (published) to evaluate the

1157 influence of $^{159}Tb^{2+}$ on Br quantification using ^{79}Br. Deviation of measured

1158 Br/published Br = 1 is found to increase with decreasing Br/Tb, reflecting the overlap

1159 of the $^{159}Tb^{2+}$ peak on ^{79}Br. USGS glasses GSE-1G and GSD-1G give relative errors

1160 of 2.5 and 1.6 %, respectively, suggesting that accurate Br determinations using ^{79}Br

1161 can be made on samples with Br/Tb ratios ≥0.6. All low Br (≤1 µg/g) glasses analysed

1162 here also have low Br/Tb ratios, contributing to measured Br/published Br > 1.

1163 Published Br data for NIST SRM 610, NIST SRM 612, GSE-1G, GSD-1G and

1164 BHVO2-G from Marks et al. (2016), with ATHO-G and StHs6/80-G from

1165 combustion ion chromatography (this study, Table 3). Tb values for NIST SRM 610

1166   and NIST SRM 612 from Jochum et al. (2011), ATHO-G and StHs6/80-G from

1167   Jochum et al. (2006), BHVO-2G, GSE-1G and GSD-1G represent 'mean of new data'

1168   (GeoReM preferred values) and Durango (solution data for Dur-DCa) from Chew et

1169   al. (2016). Major element data for internal standard values of USGS glasses (Jochum

1170   et al., 2005), MPI-DING glasses (Jochum et al., 2006) and NIST SRM glasses

1171   (Jochum et al., 2011) are included in Table 3.

1172

1173   Figure 6. Plot of background corrected Cl/Si and Br/Si counts per second (cps) ratios

1174   *vs* spot size for 30, 38 and 58 µm square spots. Halogen/Si cps ratios for Cypriot

1175   olivine remain constant across the range of measured spot sizes, indicating that

1176   sample matrix loading of the plasma is likely responsible for the apparent positive

1177   halogen signals observed in halogen-free olivine (we estimate a nominal olivine Cl

1178   value of 0.3 µg/g based on a glass Cl content of 260 µg/g (Portnyagin et al., 2002) and

1179 $D_{Cl}^{ol/melt} = 0.0012$ (Dalou et al., 2012; Fabbrizio et al., 2013)). For smaller spot sizes,

1180   the propagated uncertainties on halogen/Si ratios are appreciably larger, reflecting

1181   lower measured signal intensities.

1182

1183   Figure 7. Internal standard normalised fractionation index values (FI$_{43,}$ normalised to

1184 ^{43}Ca) for LA-ICP-MS measurements on reference glasses, apatites and scapolites at

1185   (a) 25 Hz for 30, 38 and 58 µm square spots and (b) 50 Hz for 58 µm square spots.

1186   Faint symbols denote post halogen-free correction ^{35}Cl FI$_{43}$ values for low Cl glasses

1187   GSD-1G and NIST SRM 612. With increasing analyte volatility, no systematic

1188   variation in fractionation index is observed; almost all values plotting within 10% of

1189   unity, the majority within 5%. For all SRMs and spot sizes the average FI$_{43}$ is 1.01

1190 (range 0.92 – 1.12), suggesting time-dependent fractionation is negligible for our

1191 analytical set-up.

1192

1193 Figure 8. Plot of bias (accuracy) *vs* 2 RSD (precision) for (a) Cl determinations using

1194 58 µm square spots. MPI-DING glasses KL2-G, ML3B-G, GOR128-G and GOR132-

1195 G are omitted on account of their low Cl contents that are below the limit of

1196 quantification. See Table 3 for number of replicates (*n*) for each reference material.

1197 Durango data represent analyses on in-house c-axis parallel crystal slab. R6600

1198 scapolite reference value from (van der Zwan et al., 2012). Published values for

1199 ATHO-G and StHs6/80-G from CIC analysis (this study). (b) Br determinations using

1200 58 µm square spots for reference glasses GSE-1G and GSD-1G and gem scapolites

1201 SY, SP and BB1 for which published Br data are available and above the limit of

1202 quantification for LA-ICP-MS analysis.

1203

1204 Figure 9. LA-ICP-MS data (this study) *vs* published data for (a) ^{35}Cl (see Table 1 for

1205 published data). Prior to correction using the 'nominally halogen-free' method, the

1206 marked deviation from the 1:1 line shown by low Cl glasses (faint symbols) suggests

1207 a limit of quantification of ~ 400 µg/g, in agreement with the theoretical LOQ of 360

1208 µg/g Cl (calculated using Eq. 1 and reference materials with >700 µg/g Cl). Once

1209 corrected, all low-Cl glasses plot within error of published values (except GOR132-G,

1210 information value). Glass limit of linearity was estimated through deviation from the

1211 1:1 line for corrected LA-ICP-MS *vs* published data. (b) ^{79}Br. Materials with >30 µg/g

1212 Br show excellent agreement between LA-ICP-MS (this study) and published values.

1213 For glasses, the magnitude of Br excess using ^{79}Br inversely correlates with the Br/Tb

1214 of the reference material (Fig. 5) due to contributions form ^{159}Tb^{2+} (Fig. 4b). NIST

1215   SRM 610 (437 µg/g Tb) returns elevated Br using ^{79}Br (33 ± 4 µg/g, Seo et al. (2011);

1216   36 ± 4 µg/g, this study) *vs* 0.24 µg/g via the NG method (Marks et al., 2016).

1217   Theoretical limit of quantification (LOQ) for Br (8 µg/g) calculated using Eq. 1 and

1218   data for SRMs with >32 µg/g Br. Shaded field (5 – 20 µg/g Br) represents range with

1219   a lack of well characterised, homogeneous SRMs, inhibiting testing of the theoretical

1220   LOQ, however the 'A' and 'RD' glasses of Cadoux et al., 2017 have suitable Br

1221   contents (~10 µg/g), and in the case of 'A' high Br/Tb (9.4), making them ideal for

1222   further analytical investigations. Low Br/Tb in the low Br glasses analysed here

1223   makes an assessment of the limit of linearity for Br difficult, but we estimate it to be ~

1224   2 µg/g and could be better constrained with a greater availability of suitable well

1225   characterised reference materials. Average limits of detection (LOD) calculated

1226   following Longerich et al. (1996).

1227

1228   Figure 10. Measured Cl concentrations in reference materials *vs* ablation spot

1229   size/area for a series of 10 analyses per spot size (30, 38, 58, 80 µm). (a) 1000 –

1230   100000 µg/g Cl; The excellent accuracy and reproducibility for the gem quality

1231   scapolites is maintained across all spot sizes. Smithsonian scapolite R6600

1232   consistently returns higher Cl contents than the results of van der Zwan et al. (2012),

1233   with our data showing closer agreement with the measurements of Jarosewich et al.

1234   (1980). Durango and 815 apatites represent ideal reference standards for all spot sizes.

1235   Madagascar shows inferior accuracy (bias = 12.6 %) that likely reflects, in part,

1236   sample heterogeneity across the multiple gem roughs analysed here. (b) 200 – 2000

1237   µg/g Cl; All intermediate Cl glasses (except ATHO-G) plot well within error of

1238   published values across the range of spot sizes. Glass GSD-1G provides the most

1239   consistent results across all spot sizes and is our preferred low-Cl glass reference

1240 material. (c) 20 – 200 µg/g Cl; Ultralow-Cl (~50 µg/g) glasses show unacceptably

1241 high errors (32 – 39 % 2 RSD), indicating that this likely represents an estimate of the

1242 limit of detection of the technique. Error bars represent 2 σ uncertainties. Where

1243 standard ranges overlap strongly (panel c), standard fields are discontinuous to aid

1244 visualisation. The majority of analyses for this study were performed at 58 µm, Table

1245 3.

1246

1247 Figure 11. Measured Br concentrations (a) 200 – 900 µg/g; (b) 10 – 60 µg/g *vs*

1248 ablation spot size/area. Bromine determinations for scapolites SY and SP are

1249 comparable for spots of 30 – 80 µm, plotting at the upper bounds of their respective

1250 published data ranges. Scapolite BB1 also yields similar Br values for all spot sizes,

1251 but at the lower end of the published field. Glasses GSE-1G and GSD-1G yield data

1252 within error of the published range for all spot sizes, however averages of 30 and 38

1253 µm spot results plot at the lower limits. For all reference materials, ^{81}Br

1254 determinations show closer agreement with known values, a feature that is most

1255 pronounced for glasses measured using larger spot sizes (58 and 80 µm). Figure 1

1256 shows clear evidence for the impingement of the low mass tail of $^{40}Ar^{40}Ar$ on ^{79}Br,

1257 whilst Figure 7 supports the theory that the magnitude of the excess positive Br signal

1258 scales with sample matrix input. Accordingly, the improved accuracy of ^{81}Br

1259 measurements relative to ^{79}Br, particularly at larger spot sizes, is inferred to reflect an

1260 increase in the extent of $^{40}Ar^{40}Ar$ peak broadening as a result of reduced ionisation

1261 efficiency of the plasma. Error bars represent 2σ uncertainties. Note, no published Br

1262 data are available for Smithsonian scapolite R6600.

1263

1264 Figure 12. Comparison of LA-ICP-MS and EPMA Cl data for closely spaced

1265 transects (100 – 150 μm apart) across the widths of seven large (2 – 5 mm length)

1266 apatite crystals hosted in sub-volcanic lamprophyre from the Iberian Chain, Central

1267 Spain (Galé Bornao, 2005). The largest crystals were analysed using 58 μm square

1268 spots, with 38 and 30 μm spots used for smaller grains. n represents the ratio of the

1269 number of EPMA spots (red) to LA-ICP-MS spots (black) used to define comparative

1270 transects for each crystal at a given spot size. The lamprophyre apatite LA-ICP-MS

1271 data agree within 0.5 – 7.3 % of the electron microprobe results. The greatest

1272 disparity is observed for 58 μm laser spots (2.2 – 7.3 % bias), indicating that the scale

1273 of Cl heterogeneity in the apatites is present at a smaller scale. Close agreement

1274 between the two methods for 30 and 38 μm laser spots (0.5 – 0.9 % bias), suggests

1275 that Cl is homogeneously distributed within the apatite grains at the 10 – 40 μm scale.

1276

1277 References

1278 Adlington, L., 2017. The Corning Archaeological Reference Glasses: New Values
1279   for "Old" Compositions. Papers from the Institute of Archaeology, 27(1).
1280 Aiuppa, A., Baker, D., Webster, J., 2009. Halogens in volcanic systems. Chemical
1281   Geology, 263(1): 1-18.
1282 Ansberque, C., Mark, C., Caulfield, J.T., Chew, D.M., 2019. Combined in-situ
1283   determination of halogen (F, Cl) content in igneous and detrital apatite by
1284   SEM-EDS and LA-Q-ICPMS: A potential new provenance tool. Chemical
1285   Geology.
1286 Baasner, A., Schmidt, B., Webb, S., 2013. Compositional dependence of the
1287   rheology of halogen (F, Cl) bearing aluminosilicate melts. Chemical
1288   Geology, 346: 172-183.
1289 Balcone-Boissard, H., Michel, A., Villemant, B., 2009. Simultaneous Determination
1290   of Fluorine, Chlorine, Bromine and Iodine in Six Geochemical Reference
1291   Materials Using Pyrohydrolysis, Ion Chromatography and Inductively
1292   Coupled Plasma-Mass Spectrometry. Geostandards and Geoanalytical
1293   Research, 33(4): 477-485.
1294 Balcone‐Boissard, H., Villemant, B., Boudon, G., 2010. Behavior of halogens
1295   during the degassing of felsic magmas. Geochemistry, Geophysics,
1296   Geosystems, 11(9).
1297 Bénard, A. et al., 2016. Chlorine and fluorine partition coefficients and
1298   abundances in sub-arc mantle xenoliths (Kamchatka, Russia):

1299 Implications for melt generation and volatile recycling processes in
1300 subduction zones. Geochimica et Cosmochimica Acta.
1301 Bernini, D., Wiedenbeck, M., Dolejš, D., Keppler, H., 2013. Partitioning of halogens
1302 between mantle minerals and aqueous fluids: implications for the fluid
1303 flow regime in subduction zones. Contributions to Mineralogy and
1304 Petrology, 165(1): 117-128.
1305 Beyer, C. et al., 2016. Fluorine partitioning between eclogitic garnet,
1306 clinopyroxene, and melt at upper mantle conditions. Chemical Geology,
1307 437: 88-97.
1308 Brill, R.H., 1972. A chemical-analytical round-robin on four synthetic ancient
1309 glasses, Int. Congr. Glass, Artistic Hist. Commun, 9th, pp. 93-110.
1310 Broadley, M.W., Ballentine, C.J., Chavrit, D., Dallai, L., Burgess, R., 2016.
1311 Sedimentary halogens and noble gases within Western Antarctic
1312 xenoliths: Implications of extensive volatile recycling to the sub
1313 continental lithospheric mantle. Geochimica et Cosmochimica Acta, 176:
1314 139-156.
1315 Bu, X., Wang, T., Hall, G., 2003. Determination of halogens in organic compounds
1316 by high resolution inductively coupled plasma mass spectrometry (HR-
1317 ICP-MS). Journal of Analytical Atomic Spectrometry, 18(12): 1443-1451.
1318 Bureau, H. et al., 2016. Modern and past volcanic degassing of iodine. Geochimica
1319 et Cosmochimica Acta, 173: 114-125.
1320 Bureau, H., Keppler, H., Métrich, N., 2000. Volcanic degassing of bromine and
1321 iodine: experimental fluid/melt partitioning data and applications to
1322 stratospheric chemistry. Earth and Planetary Science Letters, 183(1-2):
1323 51-60.
1324 Bureau, H., Métrich, N., 2003. An experimental study of bromine behaviour in
1325 water-saturated silicic melts. Geochimica et Cosmochimica Acta, 67(9):
1326 1689-1697.
1327 Cadoux, A. et al., 2017. A new set of standards for in–situ measurement of
1328 bromine abundances in natural silicate glasses: Application to SR-XRF,
1329 LA-ICP-MS and SIMS techniques. Chemical geology, 452: 60-70.
1330 Cadoux, A. et al., 2018. The role of melt composition on aqueous fluid vs. silicate
1331 melt partitioning of bromine in magmas. Earth and Planetary Science
1332 Letters, 498: 450-463.
1333 Chavrit, D. et al., 2016. The contribution of hydrothermally altered ocean crust to
1334 the mantle halogen and noble gas cycles. Geochimica et Cosmochimica
1335 Acta, 183: 106-124.
1336 Chew, D.M. et al., 2016. (LA, Q)-ICPMS trace-element analyses of Durango and
1337 McClure Mountain apatite and implications for making natural LA-ICPMS
1338 mineral standards. Chemical Geology, 435: 35-48.
1339 Chew, D.M., Donelick, R.A., Donelick, M.B., Kamber, B.S., Stock, M.J., 2014. Apatite
1340 Chlorine Concentration Measurements by LA‐ICP‐MS. Geostandards
1341 and Geoanalytical Research, 38(1): 23-35.
1342 Chu, M.-F. et al., 2009. Apatite composition: tracing petrogenetic processes in
1343 Transhimalayan granitoids. Journal of Petrology, 50(10): 1829-1855.
1344 Collins, S., Pyle, D., Maclennan, J., 2009. Melt inclusions track pre-eruption
1345 storage and dehydration of magmas at Etna. Geology, 37(6): 571-574.

1346 Dalou, C., Koga, K.T., Shimizu, N., Boulon, J., Devidal, J.-L., 2012. Experimental
1347   determination of F and Cl partitioning between lherzolite and basaltic
1348   melt. Contributions to Mineralogy and Petrology, 163(4): 591-609.
1349 Debret, B. et al., 2016. Volatile (Li, B, F and Cl) mobility during amphibole
1350   breakdown in subduction zones. Lithos, 244: 165-181.
1351 Eggins, S.M., Kinsley, L., Shelley, J., 1998. Deposition and element fractionation
1352   processes during atmospheric pressure laser sampling for analysis by
1353   ICP-MS. Applied Surface Science, 127: 278-286.
1354 Engvik, A.K., Golla-Schindler, U., Berndt, J., Austrheim, H., Putnis, A., 2009.
1355   Intragranular replacement of chlorapatite by hydroxy-fluor-apatite
1356   during metasomatism. Lithos, 112(3): 236-246.
1357 Epp, T. et al., 2019. Crystallographic and fluid compositional effects on the
1358   halogen (Cl, F, Br, I) incorporation in pyromorphite-group minerals.
1359   American Mineralogist: Journal of Earth and Planetary Materials, 104(11):
1360   1673-1688.
1361 Fabbrizio, A., Stalder, R., Hametner, K., Günther, D., 2013. Experimental chlorine
1362   partitioning between forsterite, enstatite and aqueous fluid at upper
1363   mantle conditions. Geochimica et cosmochimica acta, 121: 684-700.
1364 Fietzke, J., Frische, M., 2016. Experimental evaluation of elemental behavior
1365   during LA-ICP-MS: influences of plasma conditions and limits of plasma
1366   robustness. Journal of Analytical Atomic Spectrometry, 31(1): 234-244.
1367 Fietzke, J., Frische, M., Hansteen, T.H., Eisenhauer, A., 2008. A simplified
1368   procedure for the determination of stable chlorine isotope ratios (δ 37 Cl)
1369   using LA-MC-ICP-MS. Journal of Analytical Atomic Spectrometry, 23(5):
1370   769-772.
1371 Fryer, B.J., Jackson, S.E., Longerich, H.P., 1995. The design, operation and role of
1372   the laser-ablation microprobe coupled with an inductively coupled
1373   plasma; mass spectrometer (LAM-ICP-MS) in the earth sciences. The
1374   Canadian Mineralogist, 33(2): 303-312.
1375 Fusswinkel, T. et al., 2018. Combined LA-ICP-MS microanalysis of iodine,
1376   bromine and chlorine in fluid inclusions. Journal of Analytical Atomic
1377   Spectrometry, 33(5): 768-783.
1378 Galé Bornao, C., 2005. Evolución geoquímica, petrogenética y de condiciones
1379   geodinámicas de los magmatismos pérmicos de los sectores central y
1380   occidental del Pirineo. PhD. Thesis, Universidad de Zaragoza.
1381 Green, P., Duddy, I., Gleadow, A., Tingate, P., Laslett, G., 1985. Fission-track
1382   annealing in apatite: track length measurements and the form of the
1383   Arrhenius plot. Nuclear Tracks and Radiation Measurements (1982),
1384   10(3): 323-328.
1385 Guillong, M., Latkoczy, C., Seo, J.H., Günther, D., Heinrich, C.A., 2008.
1386   Determination of sulfur in fluid inclusions by laser ablation ICP-MS.
1387   Journal of Analytical Atomic Spectrometry, 23(12): 1581-1589.
1388 Hammerli, J., Rusk, B., Spandler, C., Emsbo, P., Oliver, N.H., 2013. In situ
1389   quantification of Br and Cl in minerals and fluid inclusions by LA-ICP-MS:
1390   a powerful tool to identify fluid sources. Chemical Geology, 337: 75-87.
1391 Harlov, D.E., 2015. Apatite: A fingerprint for metasomatic processes. Elements,
1392   11(3): 171-176.
1393 Harris, D.C., 2010. Quantitative chemical analysis. Macmillan.

1394 Hedenquist, J.W., Lowenstern, J.B., 1994. The role of magmas in the formation of
1395   hydrothermal ore deposits. Nature, 370(6490): 519-527.
1396 Heinrich, C. et al., 2003. Quantitative multi-element analysis of minerals, fluid
1397   and melt inclusions by laser-ablation inductively-coupled-plasma mass-
1398   spectrometry. Geochimica et Cosmochimica Acta, 67(18): 3473-3497.
1399 Horn, I., Günther, D., 2003. The influence of ablation carrier gasses Ar, He and Ne
1400   on the particle size distribution and transport efficiencies of laser
1401   ablation-induced aerosols: implications for LA–ICP–MS. Applied Surface
1402   Science, 207(1-4): 144-157.
1403 Jarosewich, E., Nelen, J., Norberg, J.A., 1980. Reference samples for electron
1404   microprobe analysis. Geostandards Newsletter, 4(1): 43-47.
1405 Joachim, B. et al., 2015. Experimental partitioning of F and Cl between olivine,
1406   orthopyroxene and silicate melt at Earth's mantle conditions. Chemical
1407   Geology, 416: 65-78.
1408 Jochum, K.P., Enzweiler, J., Mertz-Kraus, R., Wang, X., 2010. GGR Biennial Review:
1409   Reference Materials in Geoanalytical and Environmental Research –
1410   Review for 2008 and 2009. Geostandards and Geoanalytical Research,
1411   34(4): 353-385.
1412 Jochum, K.P. et al., 2006. MPI‐DING reference glasses for in situ microanalysis:
1413   New reference values for element concentrations and isotope ratios.
1414   Geochemistry, Geophysics, Geosystems, 7(2).
1415 Jochum, K.P. et al., 2011. Determination of reference values for NIST SRM 610–
1416   617 glasses following ISO guidelines. Geostandards and Geoanalytical
1417   Research, 35(4): 397-429.
1418 Jochum, K.P., Willbold, M., Raczek, I., Stoll, B., Herwig, K., 2005. Chemical
1419   Characterisation of the USGS Reference Glasses GSA‐1G, GSC‐1G, GSD
1420   ‐1G, GSE‐1G, BCR‐2G, BHVO‐2G and BIR‐1G Using EPMA, ID‐
1421   TIMS, ID‐ICP‐MS and LA‐ICP‐MS. Geostandards and Geoanalytical
1422   Research, 29(3): 285-302.
1423 John, T., Layne, G.D., Haase, K.M., Barnes, J.D., 2010. Chlorine isotope evidence for
1424   crustal recycling into the Earth's mantle. Earth and Planetary Science
1425   Letters, 298(1): 175-182.
1426 John, T., Scambelluri, M., Frische, M., Barnes, J.D., Bach, W., 2011. Dehydration of
1427   subducting serpentinite: implications for halogen mobility in subduction
1428   zones and the deep halogen cycle. Earth and Planetary Science Letters,
1429   308(1): 65-76.
1430 Kendrick, M.A., Arculus, R., Burnard, P., Honda, M., 2013. Quantifying brine
1431   assimilation by submarine magmas: Examples from the Galápagos
1432   Spreading Centre and Lau Basin. Geochimica et Cosmochimica Acta, 123:
1433   150-165.
1434 Kendrick, M.A. et al., 2014a. Subduction-related halogens (Cl, Br and I) and H_2O
1435   in magmatic glasses from Southwest Pacific Backarc Basins. Earth and
1436   Planetary Science Letters, 400: 165-176.
1437 Kendrick, M.A., Caulfield, J.T., Nguyen, A., Zhao, J.-x., Blakey, I., 2020. Halogen and
1438   trace element analysis of carbonate-veins and Fe-oxyhydroxide by LA-
1439   ICPMS: Implications for seafloor alteration, Atlantis Bank, SW Indian
1440   Ridge. Chemical Geology, 547: 119668.
1441 Kendrick, M.A., Jackson, M.G., Hauri, E.H., Phillips, D., 2015. The halogen (F, Cl, Br,
1442   I) and H_2O systematics of Samoan lavas: Assimilated-seawater, EM2 and

1443 high-3 He/4 He components. Earth and Planetary Science Letters, 410:
1444 197-209.

1445 Kendrick, M.A. et al., 2014b. Contrasting behaviours of CO 2, S, H 2 O and
1446 halogens (F, Cl, Br, and I) in enriched-mantle melts from Pitcairn and
1447 Society seamounts. Chemical Geology, 370: 69-81.

1448 Kendrick, M.A., Kamenetsky, V.S., Phillips, D., Honda, M., 2012a. Halogen
1449 systematics (Cl, Br, I) in mid-ocean ridge basalts: a Macquarie Island case
1450 study. Geochimica et Cosmochimica Acta, 81: 82-93.

1451 Kendrick, M.A., Woodhead, J.D., Kamenetsky, V.S., 2012b. Tracking halogens
1452 through the subduction cycle. Geology, 40(12): 1075-1078.

1453 Köhler, J., Schönenberger, J., Upton, B., Markl, G., 2009. Halogen and trace-
1454 element chemistry in the Gardar Province, South Greenland: subduction-
1455 related mantle metasomatism and fluid exsolution from alkalic melts.
1456 Lithos, 113(3): 731-747.

1457 Kroslakova, I., Günther, D., 2007. Elemental fractionation in laser ablation-
1458 inductively coupled plasma-mass spectrometry: evidence for mass load
1459 induced matrix effects in the ICP during ablation of a silicate glass. Journal
1460 of Analytical Atomic Spectrometry, 22(1): 51-62.

1461 Kuisma-Kursula, P., 2000. Accuracy, precision and detection limits of SEM-WDS,
1462 SEM-EDS and PIXE in the multielemental analysis of medieval glass. X-ray
1463 Spectrometry, 29(1): 111-118.

1464 Kusebauch, C., John, T., Barnes, J.D., Klügel, A., Austrheim, H.O., 2015a. Halogen
1465 element and stable chlorine isotope fractionation caused by fluid–rock
1466 interaction (Bamble Sector, SE Norway). Journal of Petrology, 56(2): 299-
1467 324.

1468 Kusebauch, C., John, T., Whitehouse, M.J., Engvik, A.K., 2015b. Apatite as probe for
1469 the halogen composition of metamorphic fluids (Bamble Sector, SE
1470 Norway). Contributions to Mineralogy and Petrology, 170(4): 1-20.

1471 Kusebauch, C., John, T., Whitehouse, M.J., Klemme, S., Putnis, A., 2015c.
1472 Distribution of halogens between fluid and apatite during fluid-mediated
1473 replacement processes. Geochimica et Cosmochimica Acta, 170: 225-246.

1474 Ladenburger, S. et al., 2016. Compositional variation of apatite from rift-related
1475 alkaline igneous rocks of the Gardar Province, South Greenland. American
1476 Mineralogist, 101(3): 612-626.

1477 Lago, M., Arranz, E., Pocoví, A., Galé, C., Gil-Imaz, A., 2004. Lower Permian
1478 magmatism of the Iberian Chain, Central Spain, and its relationship to
1479 extensional tectonics. Geological Society, London, Special Publications,
1480 223(1): 465-490.

1481 Longerich, H.P., Jackson, S.E., Günther, D., 1996. Inter-laboratory note. Laser
1482 ablation inductively coupled plasma mass spectrometric transient signal
1483 data acquisition and analyte concentration calculation. Journal of
1484 analytical atomic spectrometry, 11(9): 899-904.

1485 Manzini, M. et al., 2017. SIMS chlorine isotope analyses in melt inclusions from
1486 arc settings. Chemical Geology, 449: 112-122.

1487 Marks, M.A., Kendrick, M.A., Eby, G.N., Zack, T., Wenzel, T., 2016. The F, Cl, Br and
1488 I Contents of Reference Glasses BHVO‐2G, BIR‐1G, BCR‐2G, GSD‐1G,
1489 GSE‐1G, NIST SRM 610 and NIST SRM 612. Geostandards and
1490 Geoanalytical Research, 41(1): 107-122.

1491 Marks, M.A. et al., 2012. The volatile inventory (F, Cl, Br, S, C) of magmatic
1492   apatite: an integrated analytical approach. Chemical Geology, 291: 241-
1493   255.
1494 McCubbin, F.M. et al., 2011. Fluorine and chlorine abundances in lunar apatite:
1495   Implications for heterogeneous distributions of magmatic volatiles in the
1496   lunar interior. Geochimica et Cosmochimica Acta, 75(17): 5073-5093.
1497 McCubbin, F.M. et al., 2015. Experimental investigation of F, Cl, and OH
1498   partitioning between apatite and Fe-rich basaltic melt at 1.0–1.2 GPa and
1499   950–1000 C. American Mineralogist, 100(8-9): 1790-1802.
1500 Michel, A., Villemant, B., 2003. Determination of Halogens (F, Cl, Br, I), Sulfur and
1501   Water in Seventeen Geological Reference Materials. Geostandards
1502   Newsletter, 27(2): 163-171.
1503 Molloy, C., Shane, P., Nairn, I., 2008. Pre-eruption thermal rejuvenation and
1504   stirring of a partly crystalline rhyolite pluton revealed by the Earthquake
1505   Flat Pyroclastics deposits, New Zealand. Journal of the Geological Society,
1506   165(1): 435-447.
1507 O'Reilly, S.Y., Griffin, W., 2000. Apatite in the mantle: implications for
1508   metasomatic processes and high heat production in Phanerozoic mantle.
1509   Lithos, 53(3): 217-232.
1510 Pagé, L., Hattori, K., de Hoog, J.C., Okay, A.I., 2016. Halogen (F, Cl, Br, I) behaviour
1511   in subducting slabs: A study of lawsonite blueschists in western Turkey.
1512   Earth and Planetary Science Letters, 442: 133-142.
1513 Paton, C., Hellstrom, J., Paul, B., Woodhead, J., Hergt, J., 2011. Iolite: Freeware for
1514   the visualisation and processing of mass spectrometric data. Journal of
1515   Analytical Atomic Spectrometry, 26(12): 2508-2518.
1516 Petrus, J., Chew, D., Leybourne, M., Kamber, B., 2017. A new approach to laser-
1517   ablation inductively-coupled-plasma mass-spectrometry (LA-ICP-MS)
1518   using the flexible map interrogation tool 'Monocle'. Chemical Geology,
1519   463: 76-93.
1520 Pettke, T. et al., 2012. Recent developments in element concentration and isotope
1521   ratio analysis of individual fluid inclusions by laser ablation single and
1522   multiple collector ICP-MS. Ore Geology Reviews, 44: 10-38.
1523 Portnyagin, M., Simakin, S., Sobolev, A., 2002. Fluorine in primitive magmas of the
1524   Troodos Ophiolite complex, Cyprus: analytical methods and main results.
1525   Geochemistry International, 40(7): 625-632.
1526 Pyle, D., Mather, T., 2009. Halogens in igneous processes and their fluxes to the
1527   atmosphere and oceans from volcanic activity: a review. Chemical
1528   Geology, 263(1): 110-121.
1529 Roberge, M. et al., 2015. Is the transition zone a deep reservoir for fluorine?
1530   Earth and Planetary Science Letters, 429: 25-32.
1531 Rottier, B., Audétat, A., 2019. In-situ quantification of chlorine and sulfur in
1532   glasses, minerals and melt inclusions by LA-ICP-MS. Chemical Geology,
1533   504: 1-13.
1534 Sarafian, A.R., Roden, M.F., Patiño‐Douce, A.E., 2013. The volatile content of
1535   Vesta: Clues from apatite in eucrites. Meteoritics & Planetary Science,
1536   48(11): 2135-2154.
1537 Schilling, J.-G., Bergeron, M., Evans, R., Smith, J., 1980. Halogens in the mantle
1538   beneath the north atlantic [and discussion]. Philosophical Transactions of

the Royal Society of London A: Mathematical, Physical and Engineering Sciences, 297(1431): 147-178.

Schnetger, B., Muramatsu, Y., 1996. Determination of halogens, with special reference to iodine, in geological and biological samples using pyrohydrolysis for preparation and inductively coupled plasma mass spectrometry and ion chromatography for measurement. Analyst, 121(11): 1627-1631.

Seifert, W., Kämpf, H., Wasternack, J., 2000. Compositional variation in apatite, phlogopite and other accessory minerals of the ultramafic Delitzsch complex, Germany: implication for cooling history of carbonatites. Lithos, 53(2): 81-100.

Seo, J.H., Guillong, M., Aerts, M., Zajacz, Z., Heinrich, C.A., 2011. Microanalysis of S, Cl, and Br in fluid inclusions by LA–ICP-MS. Chemical Geology, 284(1): 35-44.

Shane, P., Nairn, I.A., Smith, V.C., 2005. Magma mingling in the~ 50 ka Rotoiti eruption from Okataina Volcanic Centre: implications for geochemical diversity and chronology of large volume rhyolites. Journal of Volcanology and Geothermal Research, 139(3-4): 295-313.

Smith, V., Shane, P., Nairn, I., 2010. Insights into silicic melt generation using plagioclase, quartz and melt inclusions from the caldera-forming Rotoiti eruption, Taupo volcanic zone, New Zealand. Contributions to Mineralogy and Petrology, 160(6): 951-971.

Stead, C.V., Tomlinson, E.L., Kamber, B.S., Babechuk, M.G., McKenna, C.A., 2017. Rare Earth Element Determination in Olivine by Laser Ablation‐Quadrupole‐ICP‐MS: An Analytical Strategy and Applications. Geostandards and Geoanalytical Research, 41(2): 197-212.

Stock, M.J., Humphreys, M., Smith, V.C., Johnson, R.D., Pyle, D.M., 2015. New constraints on electron-beam induced halogen migration in apatite. American Mineralogist, 100(1): 281-293.

Straub, S.M., Layne, G.D., 2003. Decoupling of fluids and fluid‐mobile elements during shallow subduction: Evidence from halogen‐rich andesite melt inclusions from the Izu arc volcanic front. Geochemistry, Geophysics, Geosystems, 4(7).

Tan, S.H., Horlick, G., 1986. Background spectral features in inductively coupled plasma/mass spectrometry. Applied Spectroscopy, 40(4): 445-460.

Teiber, H., Marks, M.A., Arzamastsev, A.A., Wenzel, T., Markl, G., 2015. Compositional variation in apatite from various host rocks: clues with regards to source composition and crystallization conditions. Neues Jahrbuch für Mineralogie-Abhandlungen: Journal of Mineralogy and Geochemistry, 192(2): 151-167.

Teiber, H. et al., 2014. The distribution of halogens (F, Cl, Br) in granitoid rocks. Chemical Geology, 374: 92-109.

van der Zwan, F.M., Fietzke, J., Devey, C.W., 2012. Precise measurement of low (< 100 ppm) chlorine concentrations in submarine basaltic glass by electron microprobe. Journal of Analytical Atomic Spectrometry, 27(11): 1966-1974.

Vanhoe, H., 1993. A review of the capabilities of ICP-MS for trace element analysis in body fluids and tissues. Journal of trace elements and electrolytes in health and disease, 7(3): 131-139.

Vicenzi, E.P., Eggins, S., Logan, A., Wysoczanski, R., 2002. Microbeam characterization of corning archeological reference glasses: new additions to the smithsonian microbeam standard collection. Journal of Research of the National Institute of Standards and technology, 107(6): 719.

Wang, L.-X., Marks, M.A., Keller, J., Markl, G., 2014. Halogen variations in alkaline rocks from the Upper Rhine Graben (SW Germany): Insights into F, Cl and Br behavior during magmatic processes. Chemical Geology, 380: 133-144.

Wang, Q., Makishima, A., Nakamura, E., 2010. Determination of fluorine and chlorine by pyrohydrolysis and ion chromatography: comparison with alkaline fusion digestion and ion chromatography. Geostandards and geoanalytical research, 34(2): 175-183.

Webster, J.D., Piccoli, P.M., 2015. Magmatic apatite: A powerful, yet deceptive, mineral. Elements, 11(3): 177-182.

Woodhead, J., Hergt, J., Shelley, M., Eggins, S., Kemp, R., 2004. Zircon Hf-isotope analysis with an excimer laser, depth profiling, ablation of complex geometries, and concomitant age estimation. Chemical Geology, 209(1-2): 121-135.

Zhang, C. et al., 2016. A practical method for accurate measurement of trace level fluorine in Mg‐ and Fe‐ bearing minerals and glasses using electron probe microanalysis. Geostandards and Geoanalytical Research, 40(3): 351-363.

Zhou, L., McKenna, C.A., Long, D.G., Kamber, B.S., 2017. LA-ICP-MS elemental mapping of pyrite: An application to the Palaeoproterozoic atmosphere. Precambrian Research.
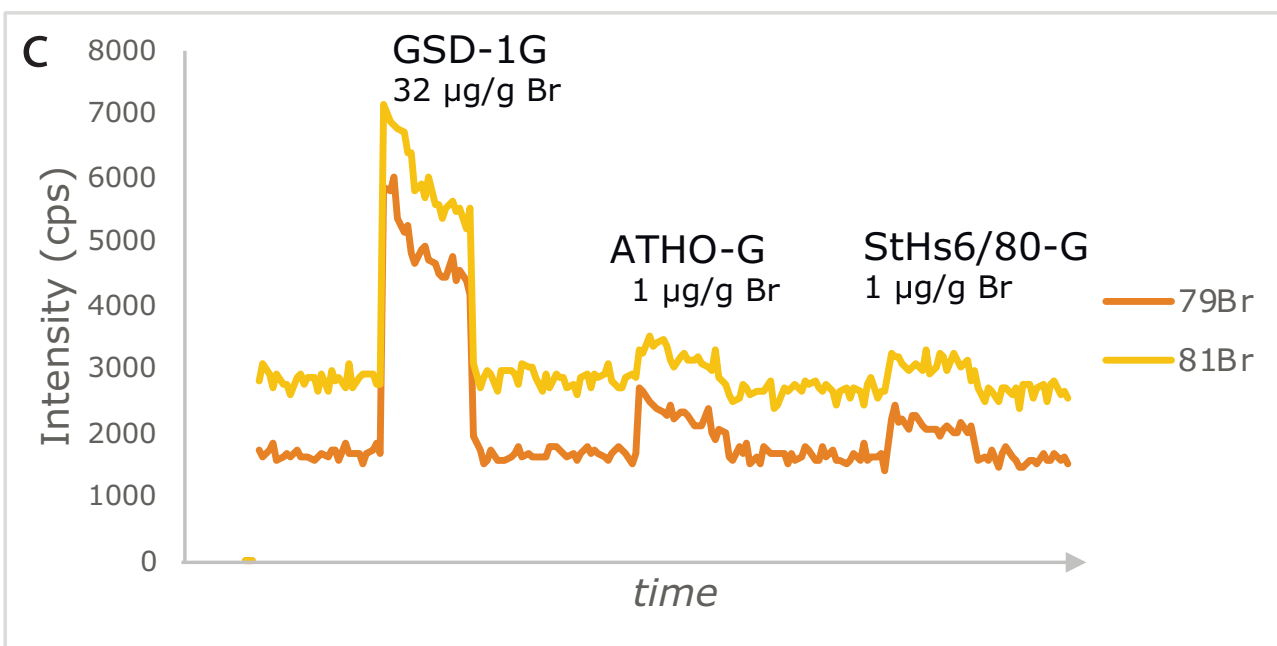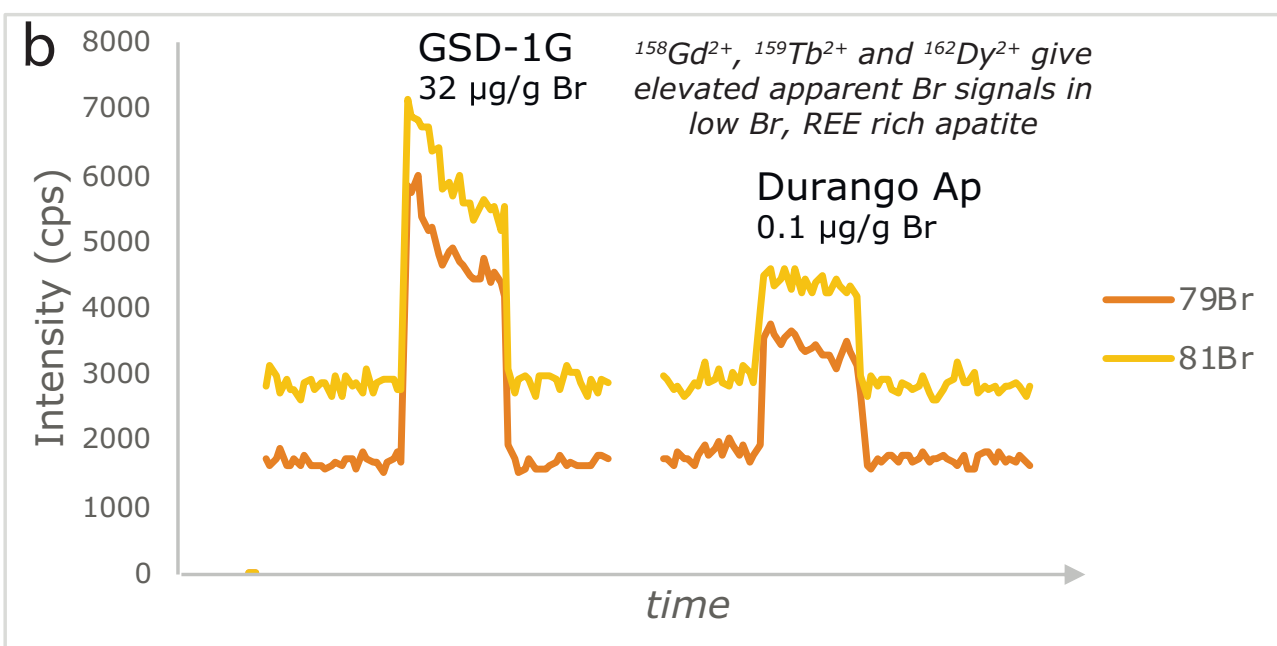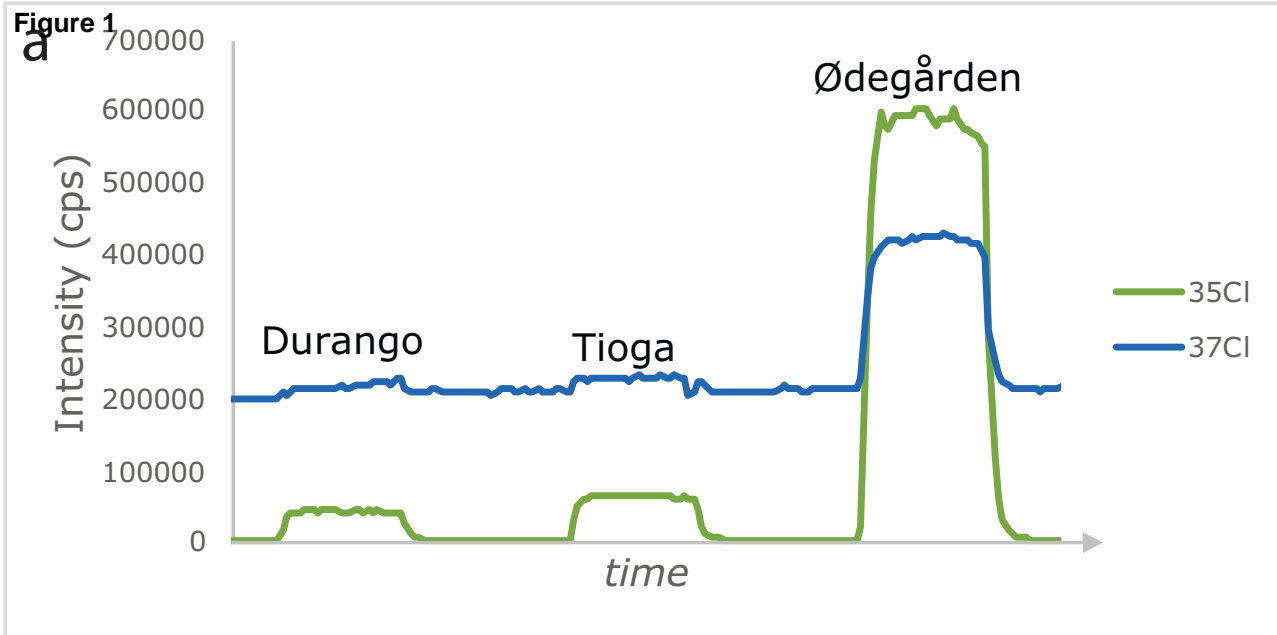
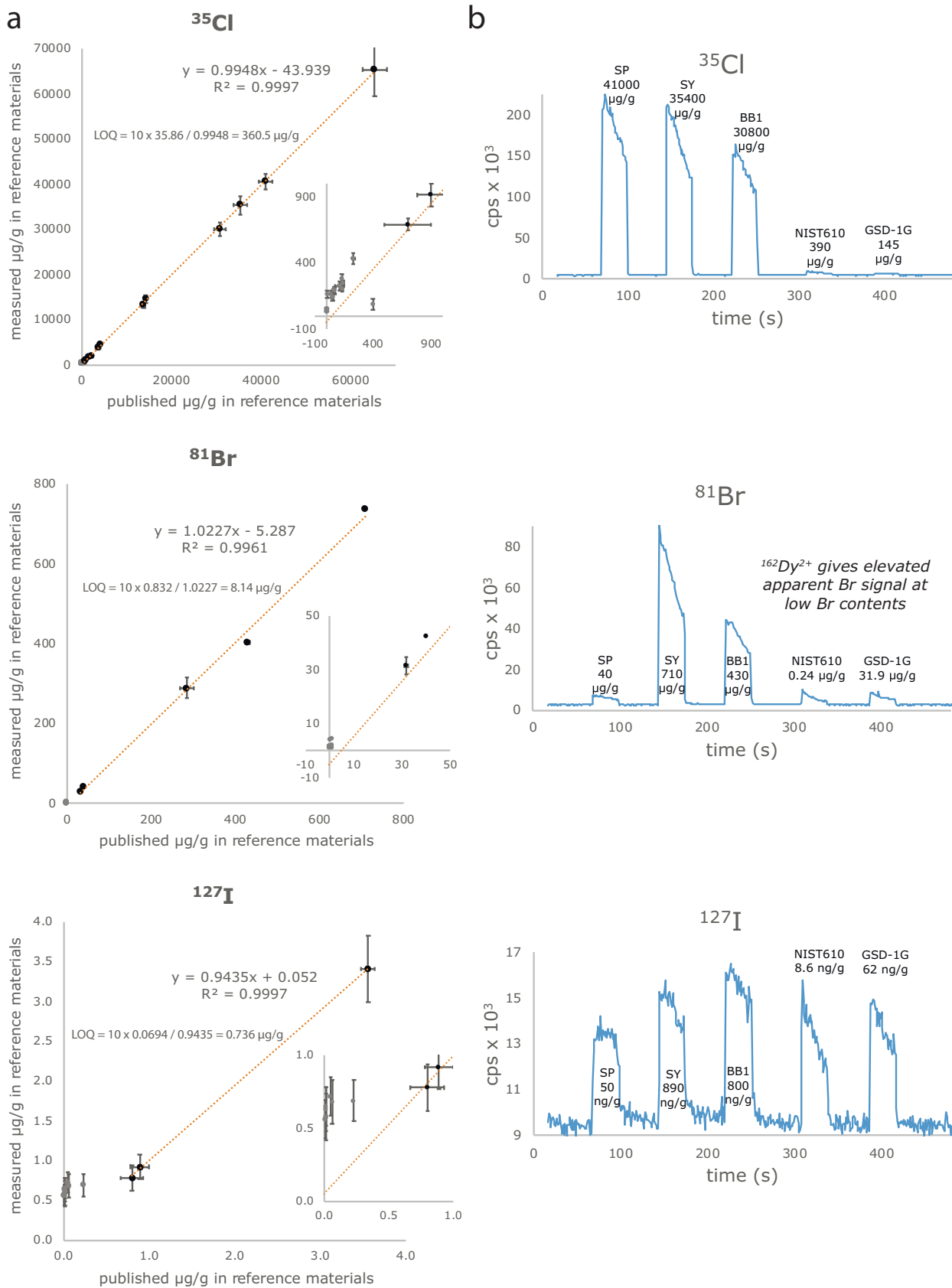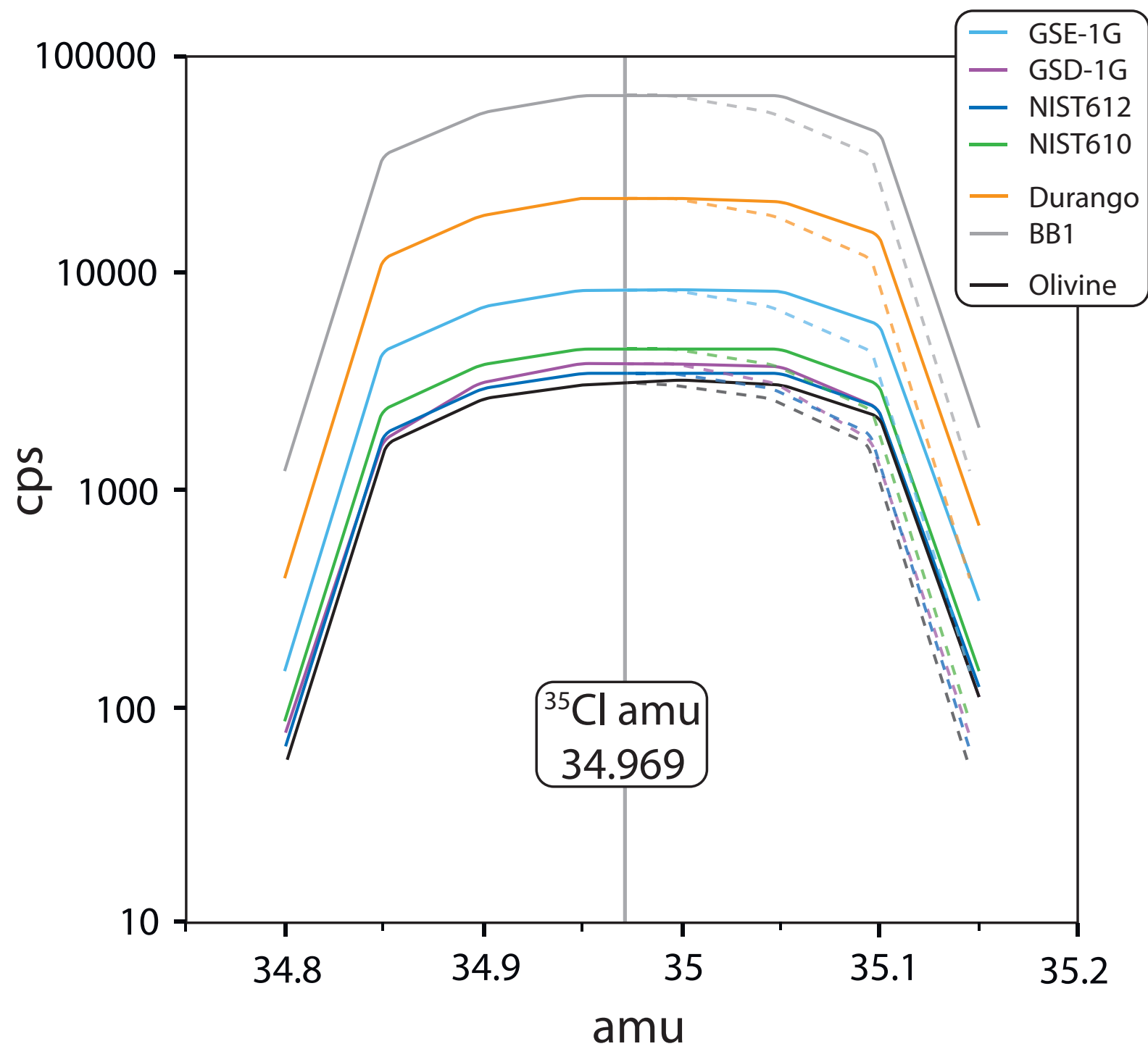**Figure 1**

Figure 1

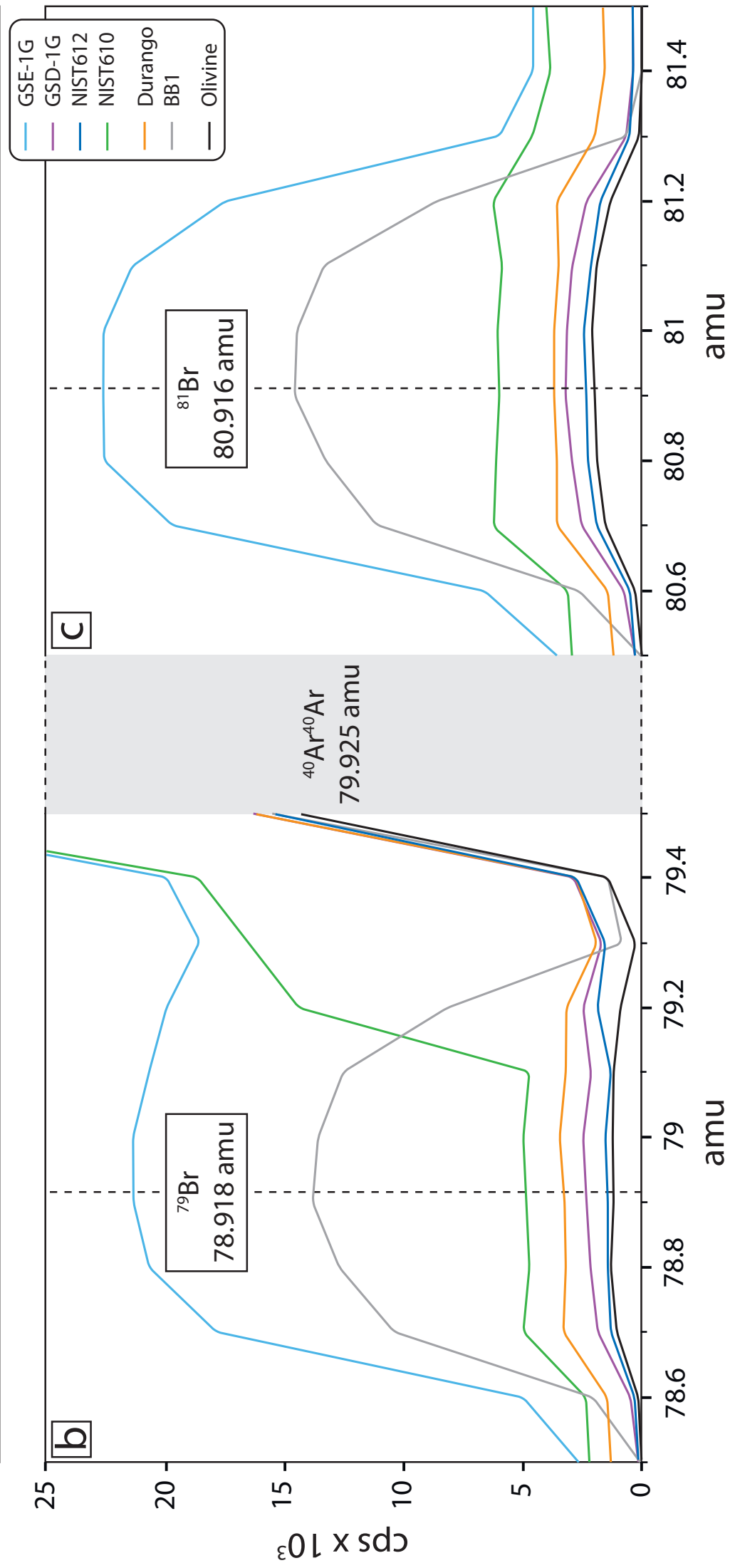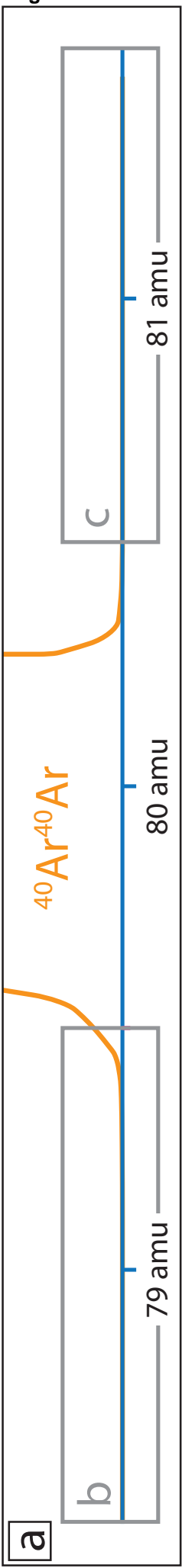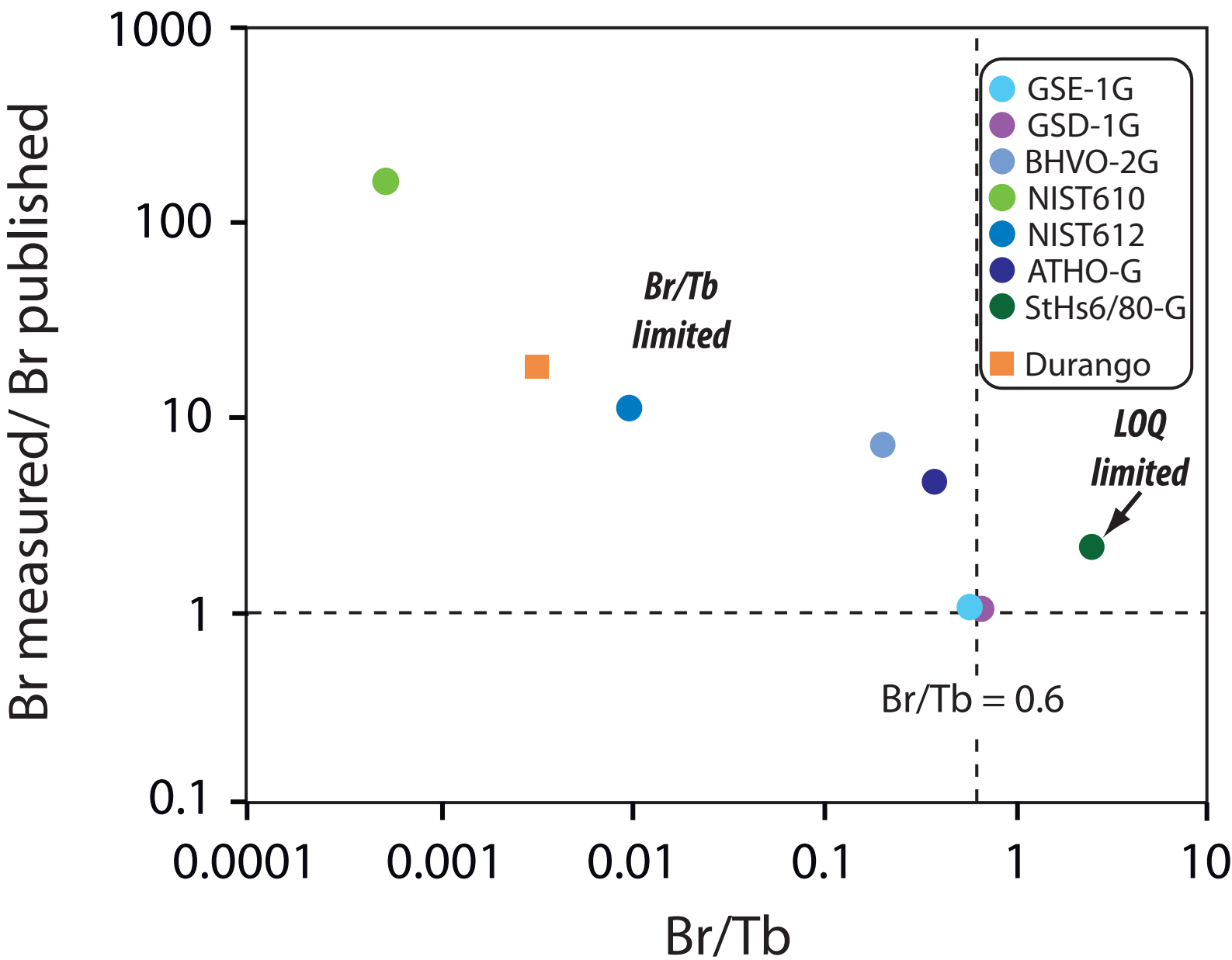**Figure 2**
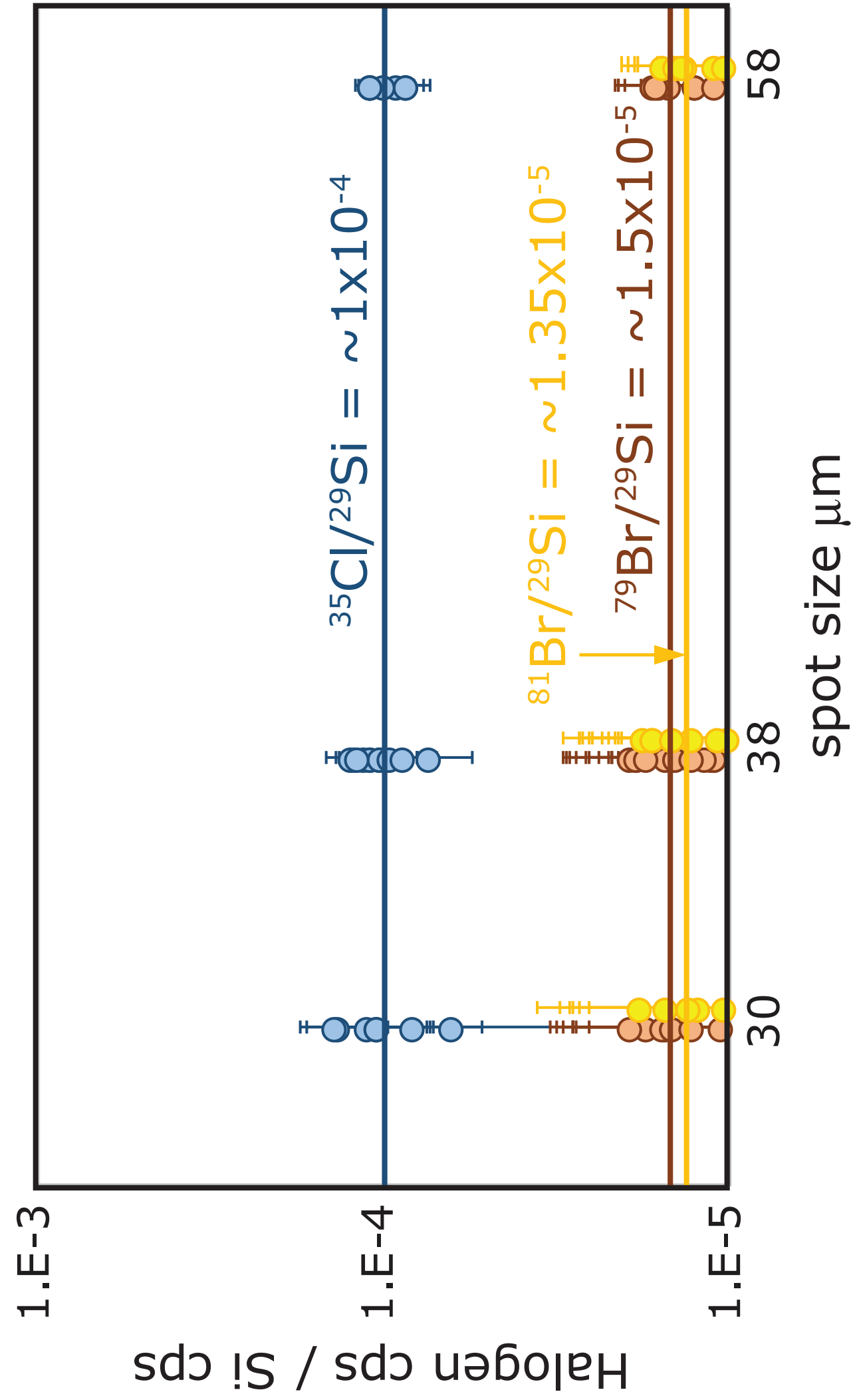

Figure 2

Figure 3

Figure 3

Figure 4

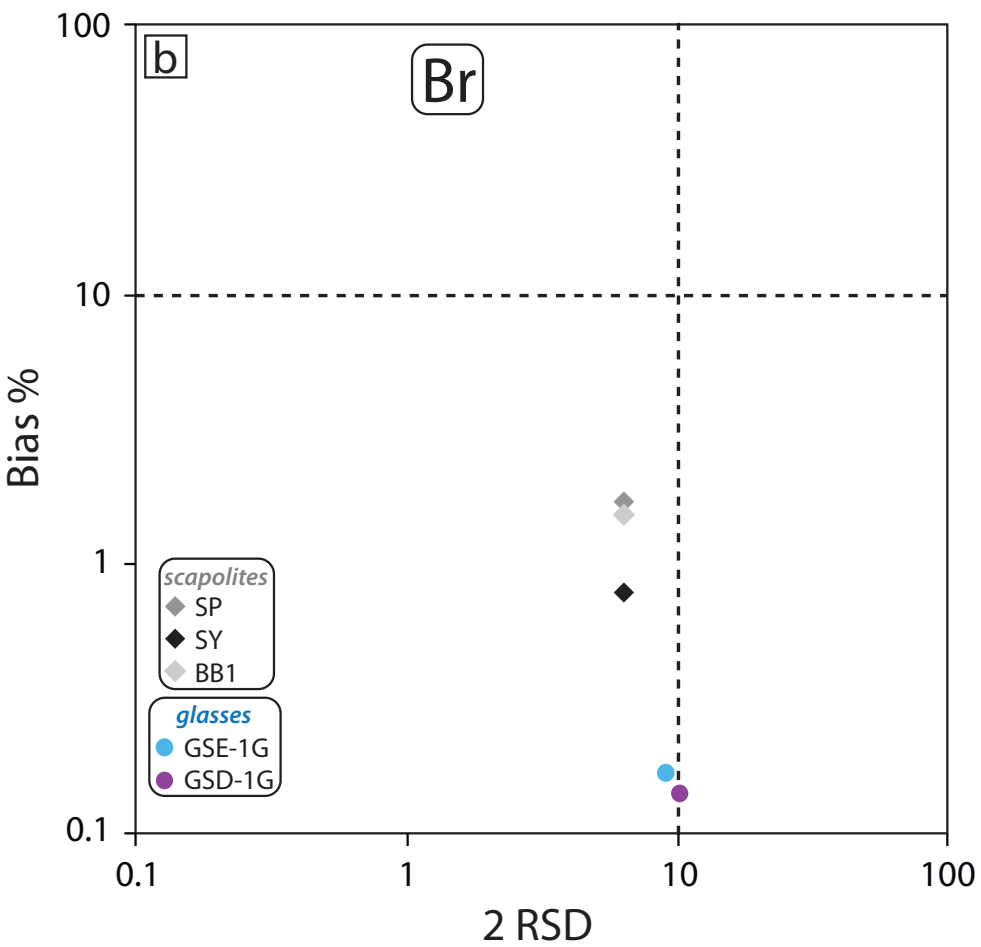Figure 4

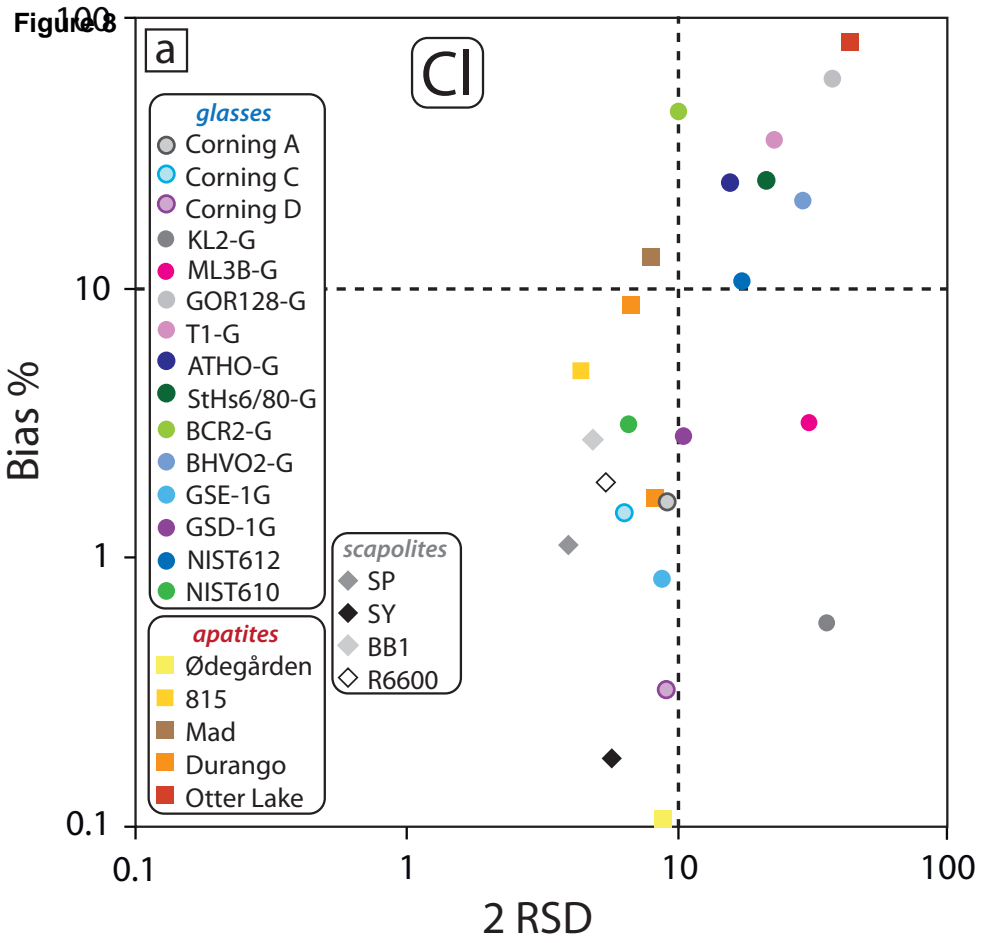Figure 5

Figure 5

Figure 6

Caulfield et al. Figure 6

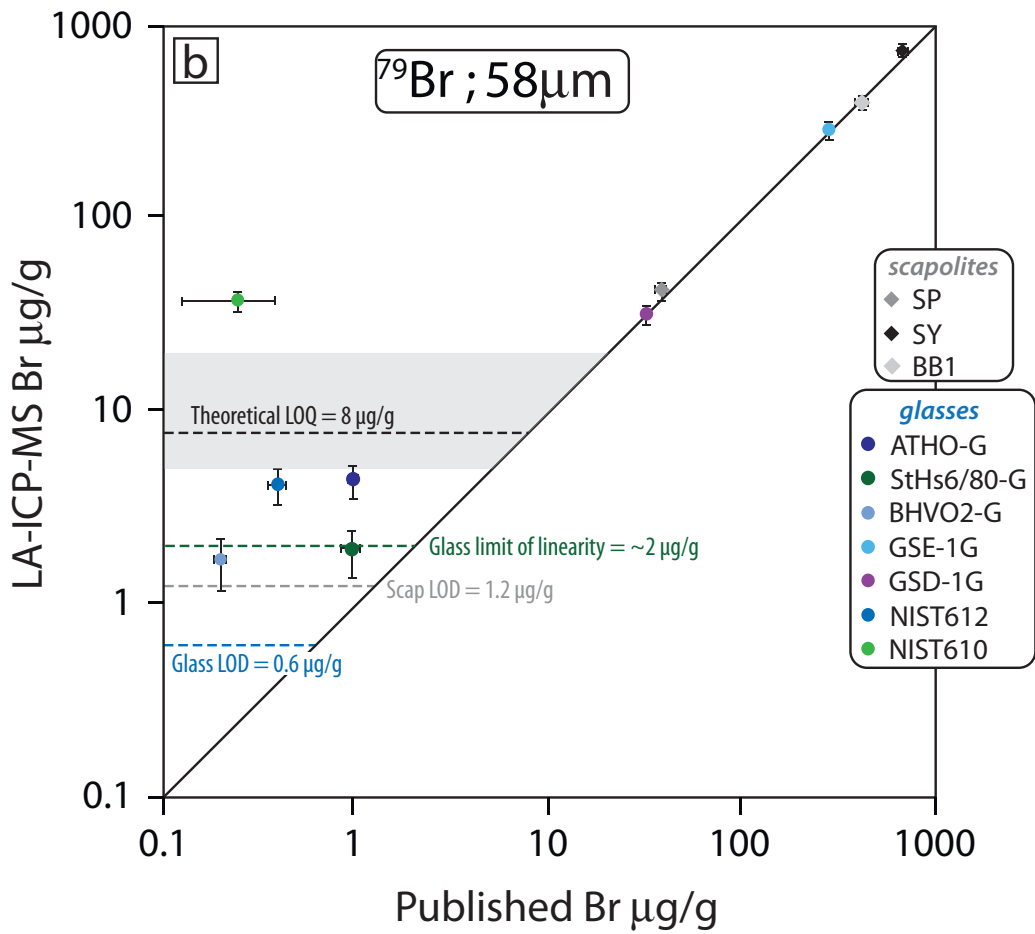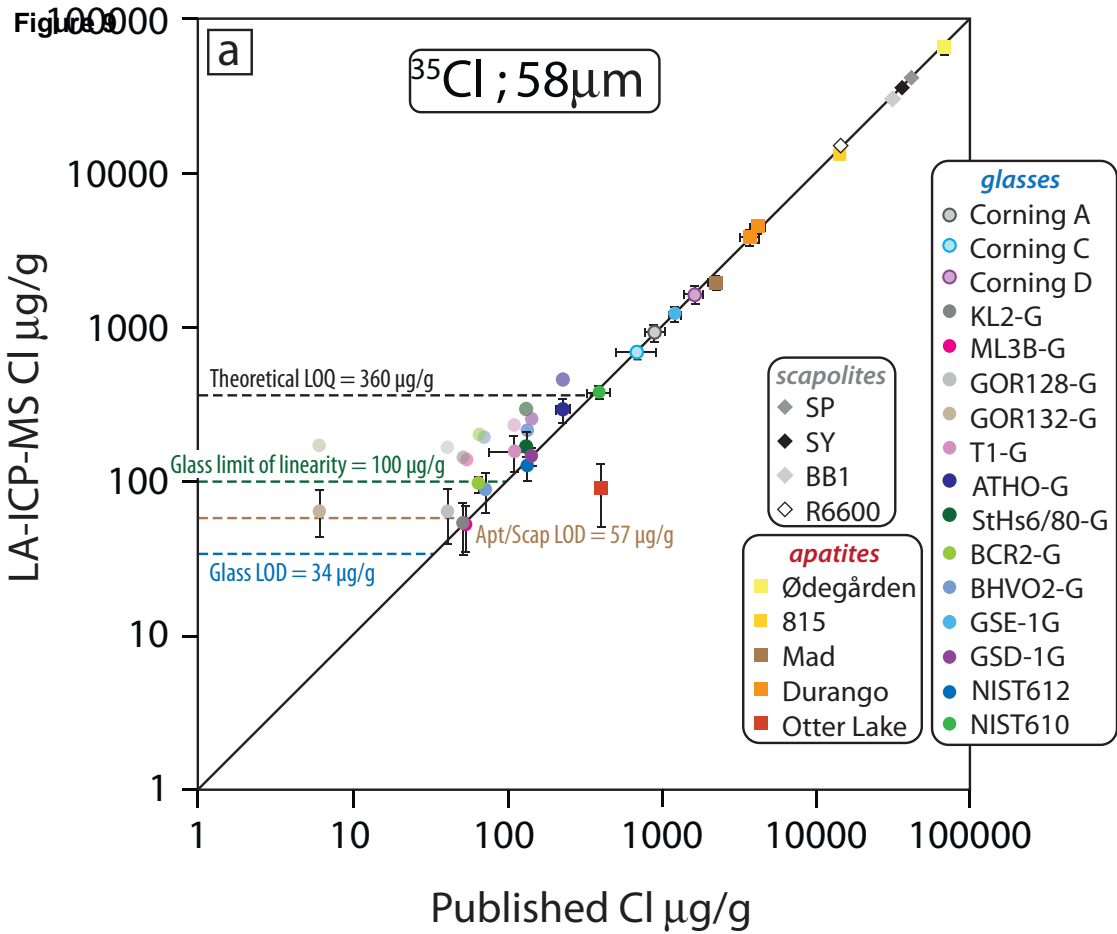Figure 7

Figure 8

Figure 8

Figure 9

Figure 9
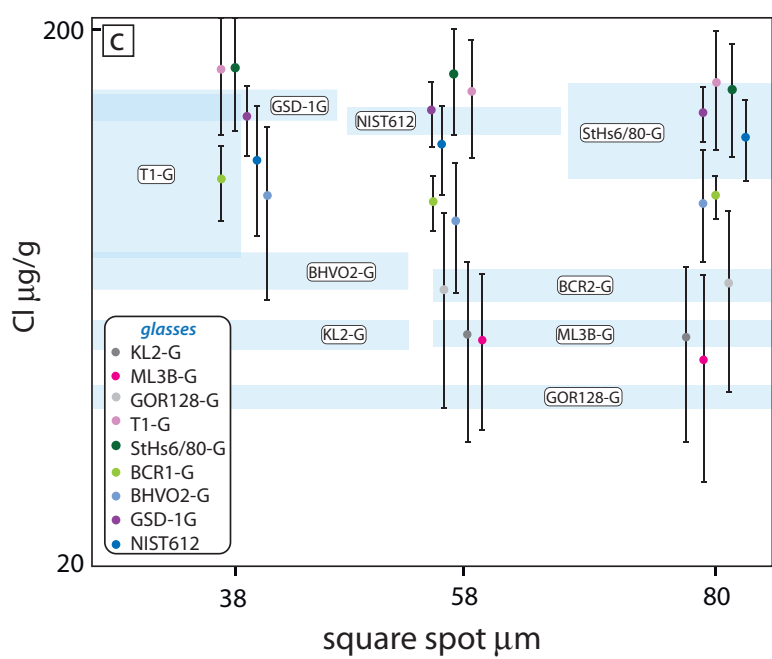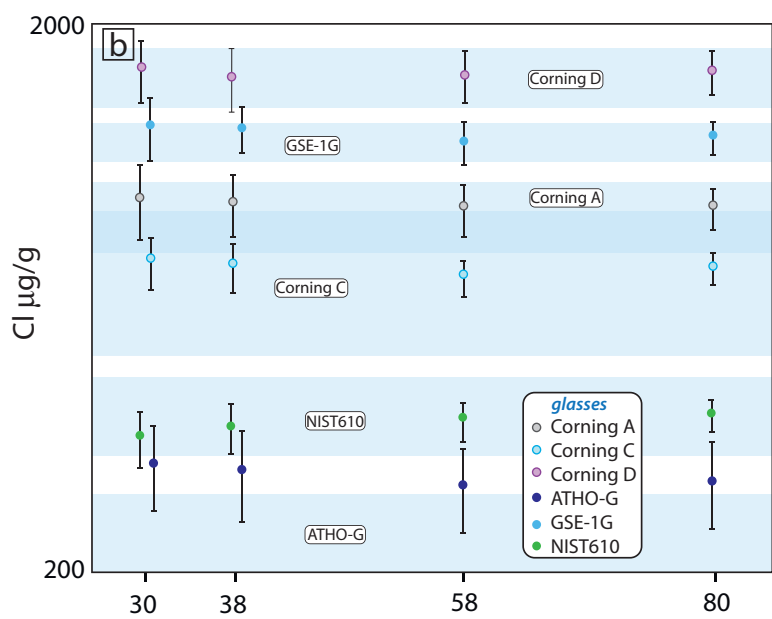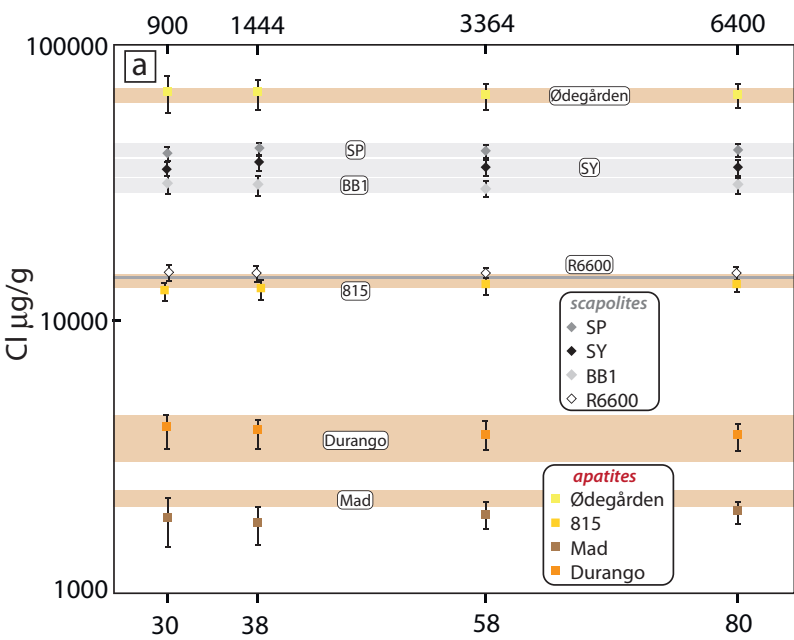
Figure 10

Figure 10

Figure 11

Figure 11

Figure 12

Figure 12

Table 1
Click here to download Table: Table 1.xlsx

Table 1. Compilation of previously reported Cl, Br and I concentrations for apatites, scapolites and reference glasses characterised in this study.

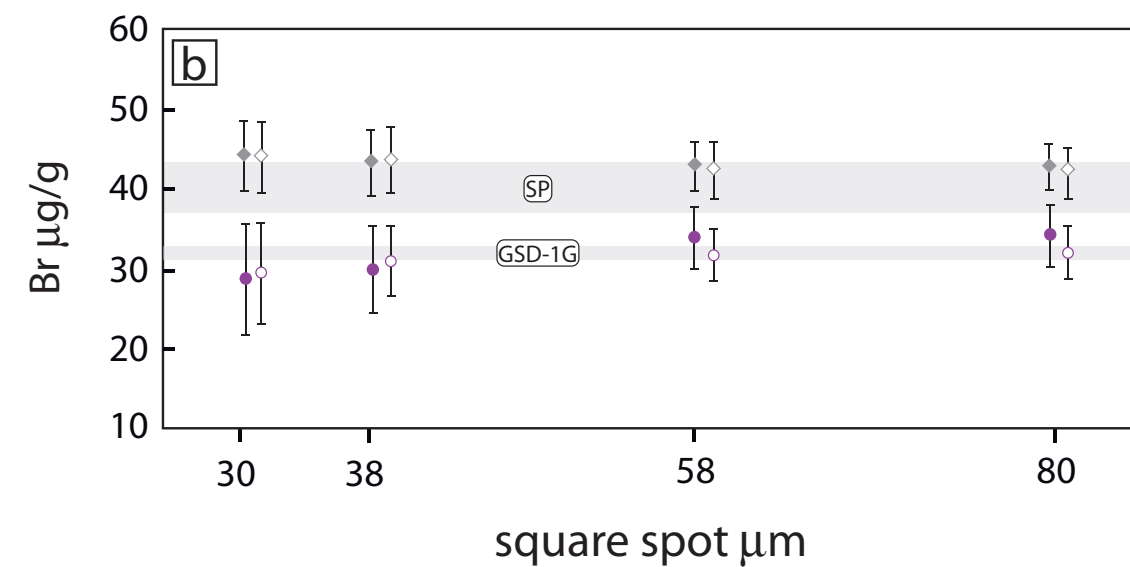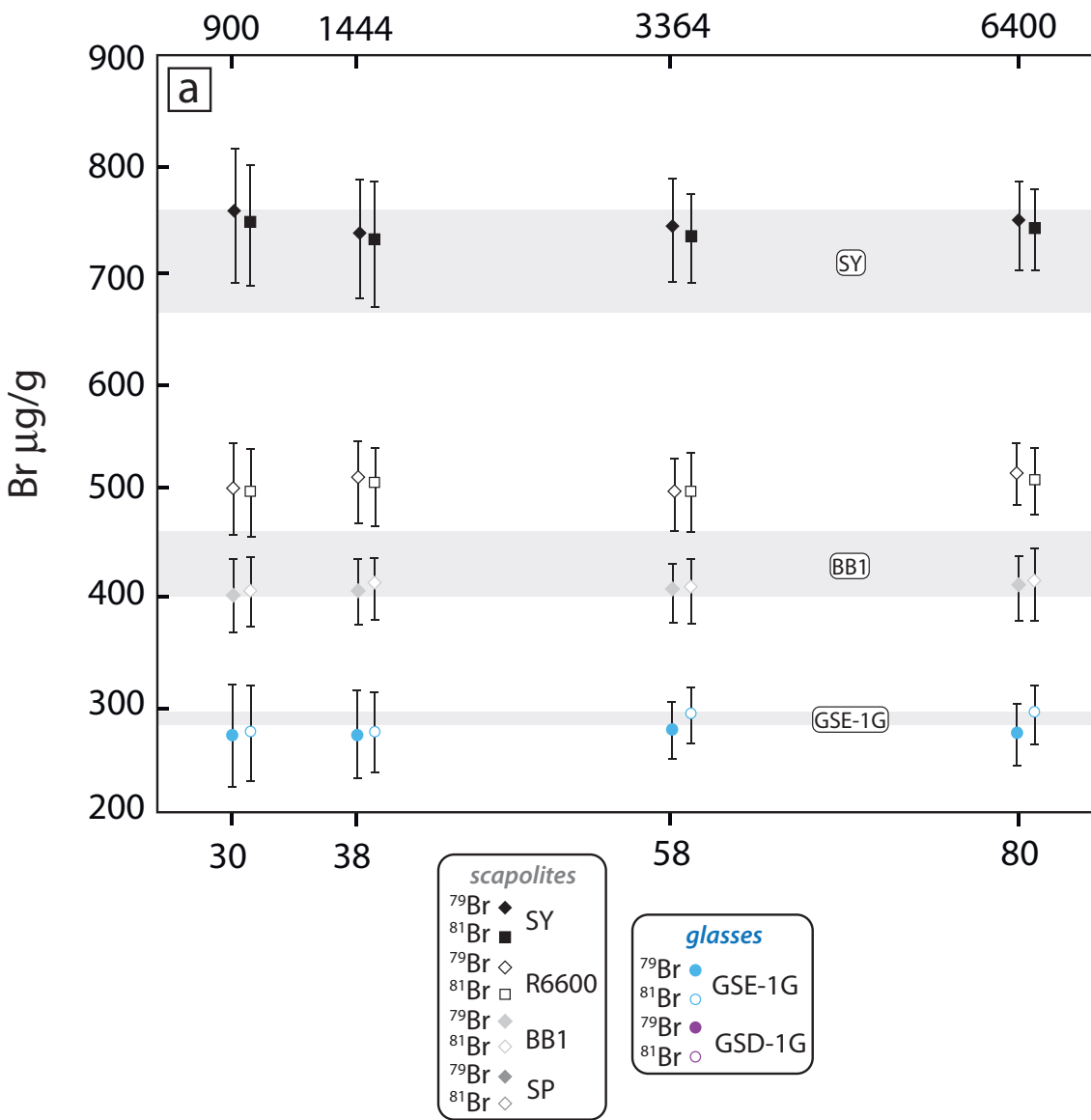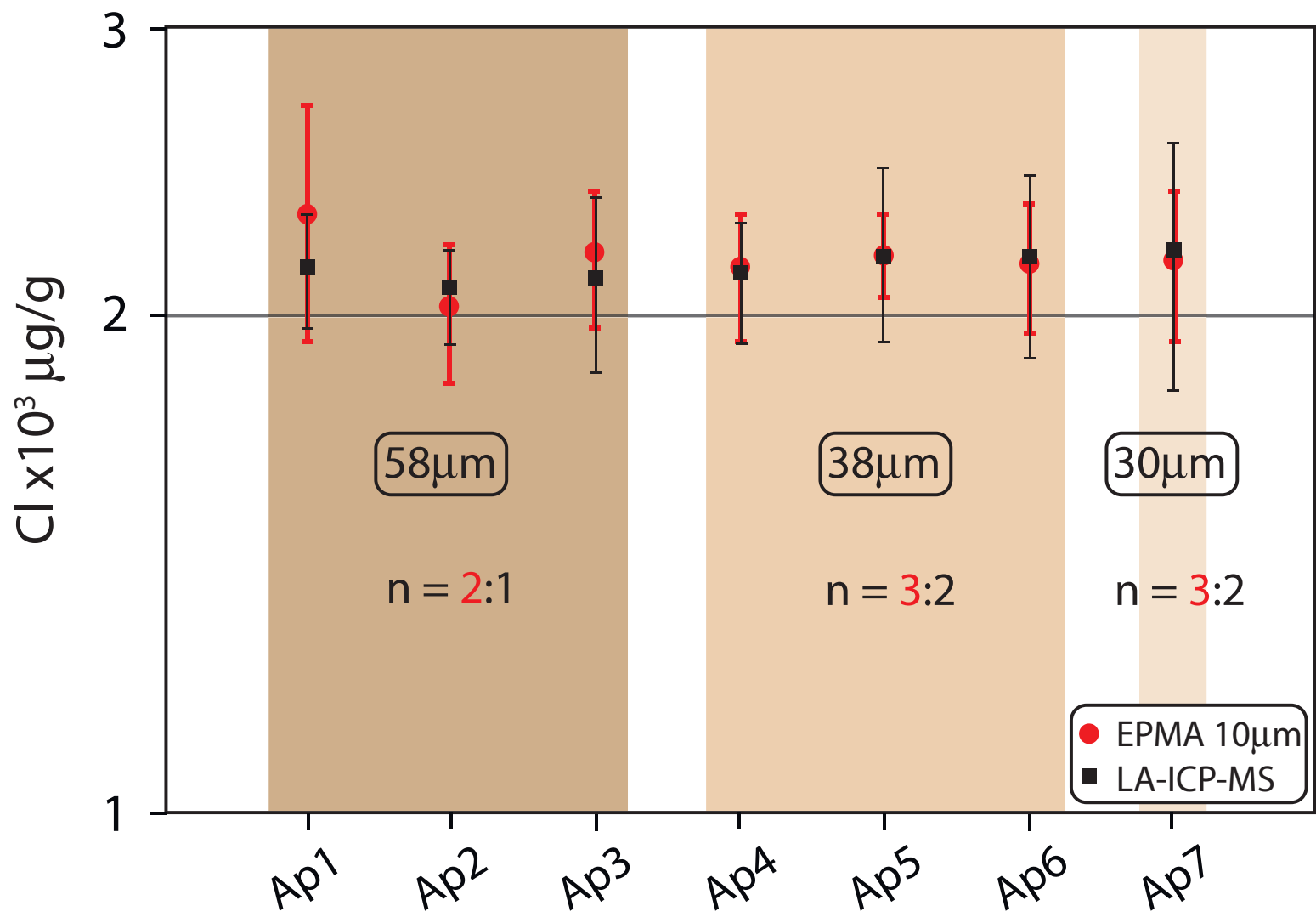| Apatites	Classification	Source	Cl µg/g	Br µg/g	I µg/g	Method	Reference
Durango	hydrothermal	TCD in-house	4600 ± 736	0.1 ± 0.05*		SIMS	Marks et al., 2012
			3700 ± 600*			EPMA	Chew et al., 2014
			4099 ± 726	0.84		PH-ICP-MS	Kusebauch et al., 2015b
			3900 ± 1000			EPMA	Kusebauch et al., 2015a
Durango NMNH 104021		Smithsonian 200 µm chips	4100*			EPMA	Jarosewich et al., 1980
Otter Lake	hydrothermal carbonate skarn	TCD in-house	400*	<0.4*		EPMA, TXRF	Teiber et al., 2015
			300 ± 200			EPMA	Carlson et al., 1999
Ødegården	metsomatic	TCD in-house	63600 ± 7632	5.9 ± 2.1*		SIMS	Marks et al., 2012
			65400 ± 2800*			EPMA	Chew et al., 2014
			64900			EPMA	Engvik et al., 2009
				23	0.23*	SIMS	Kusebauch et al., 2015a
Madagascar	silicio-carbonatitic pegmatite	TCD in-house	2200 ± 100*			LA-ICP-MS	Chew et al., 2014
815	Iron ore skarn	TCD in-house	13800 ± 400*			EPMA	Chew et al., 2014
Scapolites							
BB1	gem quality scapolite	M. Kendrick	30800 ±1300*	430 ± 30*	0.8 ± 0.13*	INAA, NG	Kendrick et al., 2013
			30700 ± 1700	533 ± 15		LA-ICP-MS	Hammerli et al., 2013
			30923 ± 4			LA-ICP-MS	Rottier & Audétat, 2019
SY	gem quality scapolite	M. Kendrick	35400 ± 1600*	710 ± 50*	0.89 ± 0.11*	INAA, NG	Kendrick et al., 2013
			34000 ± 1700	852 ± 54		LA-ICP-MS	Hammerli et al., 2013
SP	gem quality scapolite	M. Kendrick	41000 ± 1500*	40 ± 3*	0.05 ± 0.01*	INAA, NG	Kendrick et al., 2013
			39400 ± 2500	50 ± 6		LA-ICP-MS	Hammerli et al., 2013
meionite NMNH R6600		Smithsonian 200 µm chips	14300*			EPMA	Jarosewich et al., 1980
			13908 ± 49			EPMA map	van der Zwan et al., 2012
Glasses							
GSD-1G	doped basaltic glass	USGS	145 ± 8*	31.9 ± 0.4*	0.062 ± 0.002*	NG	Marks et al., 2016
GSE-1G	doped basaltic glass	USGS	1220 ± 80*	285 ± 8*	3.56 ± 0.08*	NG	Marks et al., 2016
			1330 ± 260			LA-ICP-MS	Marks et al., 2016
BHVO-2G	fused basalt	USGS	72 ± 4*	0.194 ± 0.004*		NG	Marks et al., 2016
					0.016 ± 0.004*	PH-ICP-MS	Michel and Villemant 2003
BCR-2G	fused basalt	USGS	67 ± 4*	0.090 ± 0.006		NG	Marks et al., 2016
					0.017 ± 0.008*	PH-ICP-MS	Michel and Villemant 2003
ATHO-G	fused rhyolite	MPI-DING	430	1.2 ± 0.3		SIMS, EPMA, PIXE, LIMS	Jochum et al., 2006
				1.01 ± 0.02*		SIMS	Cadoux et al., 2017
			360 ± 10			LA-ICP-MS	Rottier & Audétat, 2019
StHs6/80-G	fused andesite	MPI-DING	231 ± 50	0.8 ± 0.3		SIMS, EPMA, PIXE, LIMS	Jochum et al., 2006
				0.95 ± 0.05*		SIMS	Cadoux et al., 2017
			185 ± 35			LA-ICP-MS	Rottier & Audétat, 2019
GOR128-G	fused komatiite	MPI-DING	12[i]			SIMS, EPMA, PIXE, LIMS	Jochum et al., 2006
			41.4 ± 2*			EPMA map	van der Zwan et al., 2012
GOR132-G	fused komatiite	MPI-DING	6.2[i]*			SIMS, EPMA, PIXE, LIMS	Jochum et al., 2006
ML3B-G	fused basalt	MPI-DING	7.5[i]			SIMS, EPMA, PIXE, LIMS	Jochum et al., 2006
			54.7 ± 2.4*			EPMA map	van der Zwan et al., 2012
KL2-G	fused basalt	MPI-DING	26[i]			SIMS, EPMA, PIXE, LIMS	Jochum et al., 2006
			54.3 ± 2.7*			EPMA map	van der Zwan et al., 2012
T1-G	fused diorite	MPI-DING	113 ± 37*			SIMS, EPMA, PIXE, LIMS	Jochum et al., 2006
			148 ± 31			LA-ICP-MS	Rottier & Audétat, 2019
Corning A NMNH 117218-4	synthetic high SiO$_2$ archaeological glass	Smithsonian	900 ± 200			EPMA 40 µm beam	Vicenzi et al., 2002
			1000			nominal[a]	Vicenzi et al., 2002
			900 ± 120*			EPMA	Adlington, 2017
Corning C NMNH 117218-2	synthetic low SiO$_2$ archaeological glass	Smithsonian	700 ± 200			EPMA 40 µm beam	Vicenzi et al., 2002
			1000			nominal[a]	Vicenzi et al., 2002
			1300 ± 1000			SEM 10 µm beam	Kuisma-Kursula , 2000
			700 ± 200*			SEM 30 µm beam	Kuisma-Kursula , 2000
Corning D NMNH 117218-3	synthetic intermediate SiO$_2$ archaeological glass	Smithsonian	1600 ± 400			EPMA 40 µm beam	Vicenzi et al., 2002
			4000			nominal[a]	Vicenzi et al., 2002
			1700 ± 400			SEM 10 µm beam	Kuisma-Kursula , 2000
			1600 ± 400			SEM 30 µm beam	Kuisma-Kursula , 2000
			1600 ± 180*			EPMA	Adlington, 2017
NIST610	SRM glass	NIST	246 ± 46			LA-ICP-MS	Jochum et al., 2011
			274 ± 67			Ov. Mean	Jochum et al., 2011
				33 ± 8		LA-ICP-MS	Seo et al., 2011
			390 ± 60*	0.24 ± 0.06*	0.0086 ± 0.0014*	NG	Marks et al., 2016
			273 ± 44			PH-IC	Wang et al., 2010
			277 ± 41			LA-ICP-MS	Rottier & Audétat, 2019
NIST612	SRM glass	NIST	179			LA-ICP-MS	Jochum et al., 2011
			142 ± 58			Ov. Mean	Jochum et al., 2011
			135 ± 6*	0.39 ± 0.02*	0.0147 ± 0.001*	NG	Marks et al., 2016
			88 ± 25			PH-IC	Wang et al., 2010

Abbreviations of analytical techniques: SIMS (secondary ionisation mass spectrometry), EPMA (electron probe microanalysis), TXRF (total reflection X-ray fluorescence), LA-ICP-MS (laser ablation inductively coupled plasma mass spectrometry), INAA (instrumental neutron activation analysis), NG (noble gas), PIXE (proton induced X-ray emission), LIMS (laser plasma ionisation mass spectrometry), PH-IC (pyrohydrolysis ion chromatography), PH-ICP-MS (pyrohydrolysis inductively coupled plasma mass spectrometry). Entries from multiple techniques represent mean values.
[a]Calculated from precursor mass fractions. [i]Information values. *Denotes reference values adopted as 'known' values (this study) and for calibration where applicable. Uncertainties represent 2 sigma values.

Table 2. Instrument specifications and LA-ICP-MS running conditions.

Laser system	Teledyne Photon Machines Analyte G2 193 nm Excimer
ablation chamber	HelEx II
laser energy set point	4 mJ
laser energy density	2.75 Jcm^{-2}
repetition rate	25 & 50 Hz
spot size	30-80 µm square
signal smoothing	variable volume smoothing device set to 5 ml
acquisition time	20 s
washout	40 s
ICP-MS	Thermo Scientific iCAP Qc
MFC1 (He)	0.35 ml/min
MFC2 (He)	0.05 ml/min
MFC3 (N$_2$)	13 ml/min
nebuliser gas (Ar)	0.67 L/min
RF power	1350 W
ThO/Th (NIST612)	<0.2%
analyte dwell times (ms)	*normal resolution:* ^{35}Cl (100), ^{79}Br (250), ^{81}Br (250) ^{127}I (250), ^{208}Pb (20), ^{55}Mn (20)
	high resolution: ^{39}K (20), ^{43}Ca (20), ^{29}Si (20), ^{23}Na (20)
duty cycle	390 – 970 ms
analysis mode	standard high sensitivity mode (STDS)
tuning (NIST612)	85 µm square, 10 Hz, 2.75 Jcm^{-2}, 40 µms^{-1}

Table 3
Click here to download Table: Table 3.xlsx

Table 3. Mean Cl, Br, I, F and S concentrations of apatites, scapolites and SRM glasses determined in this study via LA-ICP-MS, EPMA and CIC.

Apatites	n =	Cl µg/g	2	Br µg/g	2	I µg/g	2	F µg/g	2	S µg/g	2	Method	CaO % m/m int. std.	SiO$_2$ % m/m int. std.	ref. for int. stds.
Durango†	38	3760	320	-		-						LA	53.84		1
	4	4400	500					33400	800			EPMA			
NMNH 104021 Durango	10	4440	310	-		-									
Otter Lake	14	90	40	-		-						LA	54		2
Ødegården	32	65330	5600	-		-						LA	52.07		1
Madagascar	32	1920	160	-		-						LA			
815	32	13150	600	-		-						LA	54.17		1
Wilberforce	5	bdl.						37900	600			EPMA			
Scapolites															
BB1	32	29980	1520	403	26	0.78	0.16					LA	7	56	3
SY	28	35340	2110	738	48	0.92	0.15					LA	5.4	56	3
SP	28	40550	1660	42.6	2.8	-						LA	1.7	62	3
NMNH R6600 meionite	14	14570	810	494	32	1.25	0.18					LA	13.58	49.78	4
Glasses															
GSC-1G*	10	55	20	-		-						LA	7.14	53	5
GSD-1G*	26	141	16	31.5	3.3	-						LA	7.21	52.5	5
GSE-1G	40	1210	110	289	26	3.41	0.42					LA	7.27	52.9	5
BHVO-2G*	12	87	26	-		-						LA	11.4	49.3	5
BCR-2G*	12	96	10	-		-						LA	7.22	54.3	5
ATHO-G*	12	286	46	-		-						LA	1.7	75.6	6
	6	231	44									CIC			
	3			0.97	0.24			804	137	26	8	CIC			
StHs6/80-G*	12	164	36	-		-						LA	5.28	63.7	6
	5	132	25	0.94	0.3					7	4	CIC			
	2							290	60			CIC			
GOR128-G*	10	65	25	-		-						LA	6.24	46.1	6
GOR132-G*	10	64	22	-		-						LA	8.45	45.5	6
ML3B-G*	10	53	17	-		-						LA	10.5	51.4	6
KL2-G*	10	54	20	-		-						LA	10.9	50.3	6
T1-G*	10	152	36	-		-						LA	7.1	58.6	6
Corning A NMNH 117218-4	12	914	87	-		-						LA	5.03	66.56	7
Corning C NMNH 117218-2	12	690	45	-		-						LA	5.07	34.87	7
Corning D NMNH 117218-3	12	1610	150	-		-						LA	14.8	55.24	7
NIST610	26	378	26	-		-						LA	11.4	69.7	8
NIST612*	14	121	22	-		-						LA	11.9	72.1	8

All LA-ICP-MS data are for 58 µm square spots. Quoted values represent mean of *n* analyses. Complete dataset is included as a supplementary data file.

*LA-ICP-MS Cl data represent mean values from olivine correction DRS in iolite using NIST612 (390 µg/g Cl) as calibration standard, except ATHO-G that was calibrated using GSE-1G (1220 µg/g Cl).

References: 1. Chew et al., 2014, 2. Carlson et al., 1999, 3. Kendrick et al., 2013, 4. Jarosewich et al., 1980, 5. Jochum et al., 2005, 6. Jochum et al., 2006, 7. Vicenzi et al., 2002, 8. Jochum et al., 2011.

Methods: LA = laser ablation ICP-MS, EPMA = electron probe microanalysis, CIC = combustion ion chromatogrphy.

†LA data acquired on same Durango chip characterised by EPMA by Chew et al., 2014, cf. Table 1. EPMA data acquired on University of Oxford in-house Durango chip.

Dash denotes below limit of quantification based on results of this study. bdl. = below detection limit. Blank field denotes not measured.

A Ca value of 40.04 % m/m was adopted for internal standardisation of all apatite analyses.

Table 4

Table 4. Summary of key ablation parameters and their impact on crater aspect ratio for different materials.
Italicised, bold entries denote conditions that produce craters with aspect ratios of ≤1:1 down to 30 micrometre spots. Deeper craters require larger spot sizes to maintain a 1:1 aspect ratio.

		Ablation parameters							
		50 Hz, 20 s, 5 ml smoothing		25 Hz, 20 s, 5 ml smoothing		20 Hz, 20 s, 5 ml smoothing		20 Hz, 18 s, 5 ml smoothing	
		1000 shots fired		500 shots fired		400 shots fired		360 shots fired	
		(700 shots integrated)*		(350 shots integrated)*		(280 shots integrated)*		(240 shots integrated)*	
	Abl. Rate	Total crater depth	Crater depth	Total crater depth	Crater depth	Total crater depth	Crater depth	Total crater depth	Crater depth
Material	(μm/pluse)	(μm)	considered (μm)	(μm)	considered (μm)	(μm)	considered (μm)	(μm)	considered (μm)
Scapolite	0.07	70	59.5	35	*29.8*	28	*23.8*	25.2	*21*
Apatite	0.105	105	89.3	52.5	44.6	42	35.7	37.8	*31.5*
Glass	0.105	105	89.3	52.5	44.6	42	35.7	37.8	*31.5*
Olivine	0.09	90	76.5	45	38.3	36	*30.6*	32.4	*27*

*For all ablations, the first and last 3 seconds of the signal are excluded for each analytical integration in Iolite.

Crater depth considered excludes the last 3 seconds of ablation only.

Caulfield_et_al_supplementary_material_text

Caulfield_et_al_supplementary_material_data

Supplementary Iolite file

Supplementary Iolite file

IoliteV3Procs_pdf

X_Trace_Elements_IS_pdf